Cortical glutamatergic projection neuron types contribute to distinct functional subnetworks

Hemanth Mohan[1,3], Xu An[1,3], Hideki Kondo[3], Shengli Zhao[1], Katherine S. Matho[3], Simon Musall[3,4], Partha Mitra[3], Z. Josh Huang[1,2,3*]

[1]Department of Neurobiology, Duke University Medical Center, Durham, NC 27710, USA
[2]Department of Biomedical Engineering, Duke University, Durham, NC 27708, USA
[3]Cold Spring Harbor Laboratory, Cold Spring Harbor, NY 11724, USA.
[4] Institute of Biological information Processing, Forschungszentrum Julich, Julich, Germany

[*]corresponding author: josh.huang@duke.edu

Abstract

The cellular basis of cerebral cortex functional architecture remains not well understood. A major challenge is to monitor and decipher neural network dynamics across broad cortical areas yet with projection neuron (PN)-type resolution in real time during behavior. Combining genetic targeting and wide-field imaging, we monitored activity dynamics of subcortical-projecting (PT^{Fezf2}) and intratelencephalic-projecting (IT^{PlxnD1}) types across dorsal cortex of mice during different brain states and behaviors. IT^{PlxnD1} and PT^{Fezf2} neurons showed distinct activation patterns during wakeful resting, spontaneous movements, and upon sensory stimulation. Distinct IT^{PlxnD1} and PT^{Fezf2} subnetworks were dynamically tuned to different sensorimotor components of a naturalistic feeding behavior, and optogenetic inhibition of subnetwork nodes disrupted specific components of this behavior. Lastly, IT^{PlxnD1} and PT^{Fezf2} projection patterns are consistent with their subnetwork activation patterns. Our results show that, in addition to the concept of columnar organization, dynamic areal and PN type-specific subnetworks are a key feature of cortical functional architecture linking microcircuit components with global brain networks.

Introduction

The cerebral cortex orchestrates high-level brain functions ranging from perception and cognition to motor control, but the cellular basis of cortical network organization remains poorly understood. Across mammalian species, the cortex consists of dozens to over a hundred cortical areas, each featuring specific input-output connections with multiple other areas, thereby forming numerous functional subnetworks of information processing [1,2]. Within each area, seminal discoveries have revealed columnar organization of neurons with similar functional properties [3,4], a foundational concept that has guided decades of cortical research [5]. Across multiple cortical layers, diverse neuron types form intricate connections with each other and with neurons in other brain regions, constituting a "canonical circuit" that is duplicated and modified across areas [6-8]. An enduring challenge is to decipher the cellular basis of cortical architecture characterized by such nested levels of organization that integrates microcircuits with global networks across spatiotemporal scales [9,10].

Among diverse cortical cell types, glutamatergic pyramidal neurons (PNs) constitute key elements for constructing the cortical architecture [7,11]. Whereas PN dendrites and local axonal arbors form the skeleton of local cortical microcircuits, their long-range axons mediate communication with other cortical and subcortical regions. Indeed, PNs can be divided based on their long-range projections into diverse types hierarchically organized into several major classes, each comprising finer grained projection types [7,12]. One major class is the pyramidal tract (PT) neurons, which gives rise to corticofugal pathways that target all subcortical regions down to the brainstem and spinal cord. Another major class is the intratelencephalic (IT) neurons, which targets other cortical and striatal regions, including those in the contralateral hemisphere. Using this connectionist framework, recent studies in rodents have achieved a comprehensive description of cortical areal subnetworks [13-15] and have begun to reveal their cellular underpinnings [16,17]. However, how these anatomically-defined networks relate to functional cortical networks remains unclear, as such studies require methods to monitor neural activity patterns in real time across large swaths of cortical territory yet with cell type resolution and in behaving animals.

Traditional fMRI methods measure brain-wide metabolic activities as a proxy of neural activity but with relatively poor spatial and temporal resolution [18,19]. Conversely, single unit recording [20] and two-photon calcium imaging [21] achieve real-time monitoring of neural activity with cellular resolution, but typically with rather limited spatial coverage. Recent advances in widefield calcium imaging provide an opportunity to monitor neural activity in real time across a wide expanse of the mouse cortex at cellular resolution [22]. However, most widefield studies to date have imaged activity either of broad neuronal classes [23-25] or of laminar subpopulations containing mixed projection types [26-30]. Thus, while these studies have offered new insights into cortical activity during different brain states, they have yet to resolve and compare activity in distinct PN projection types. In particular, how IT and PT PNs each contribute to cortical processing during different brain states and as an animal moves and processes sensory information is unknown.

We have recently generated a comprehensive genetic toolkit for targeting the hierarchical organization of PNs in mouse cerebral cortex [31]. This toolkit includes the *PlxnD1* and *Fezf2* driver lines that readily distinguish IT and PT PN types. Here, we use these two Cre-driver lines to selectively express the genetically-encoded calcium indicator GCaMP6f in IT^{PlxnD1} and PT^{Fezf2} subpopulations and carried out widefield imaging across the dorsal cortex of head-fixed mice during epochs of quiet wakefulness, spontaneous movements, sensory stimulation, anesthesia and a natural feeding behavior. We found that IT^{PlxnD1} and PT^{Fezf2} show distinct activity dynamics during quiet wakefulness, spontaneous movements, upon sensory stimulation, and under anesthesia. Furthermore, we revealed distinct IT^{PlxnD1} and PT^{Fezf2} subnetworks dynamically tuned to different components of feeding behavior, including food retrieval, coordinated mouth-hand movements and food ingestion. Optogenetic inhibition of key cortical areas in these subnetworks disrupted specific components of this behavior. Anterograde tracing of IT^{PlxnD1} and PT^{Fezf2} from these key areas revealed projection patterns that contribute to functional activation patterns of corresponding subnetworks. Together, these results demonstrate that IT and PT subpopulations form parallel cortical processing streams and output pathways with spatiotemporal activity patterns that are distinct and that change dynamically and differentially with behavioral state. Consequently, in addition to the concept of columnar organization, these experiments reveal that dynamic PN type subnetworks are a key feature of cortical functional architecture that integrates cortical microcircuits to global brain networks.

Results

Although wide-field mesoscopic calcium imaging in rodents has the potential to reveal the cellular basis of functional cortical networks, the full realization of this potential critically depends on the resolution for distinguishing different PN types through specific expression of genetic encoded calcium sensors. To date, most if not all these studies examined subpopulation (e.g. those defined by Thy1 and Rbp4 transgenic lines) comprising mixtures of different projection classes [27-30], which precluded a direct and clear link between projection and function defined cortical networks. We have recently generated gene knockin mouse driver lines that enable specific genetic access to hierarchical PN classes and subpopulations within each class [31]. Among these, the *Fezf2-CreER* line captures the large majority of PT population (PT^{Fezf2}) in layer 5b and 6, and the *PlxnD1-CreER* captures an IT subpopulation (IT^{PlxnD1}) which resides in both L2/3 and L5a. Whereas PTs^{Fezf2} project to mostly ipsilateral subcortical regions and represent over 95% of corticospinal projection neurons, ITs^{PlxnD1} project to ipsi- and contra-lateral cortical and striatal targets [31]. As IT is the largest and most diverse PyN class comprising intracortical, callosal, and cortico-striatal PyNs across layer 2-6, using double mRNA in situ hybridization we estimated that *PlxnD1* represent about 63% of IT neurons marked by *Satb2* (Fig. 1b). Quantification of cell distribution using serial two-photon tomography (STP) and CCF (mouse brain Common Coordinate Framework) registration demonstrated that PT^{Fezf2} and IT^{PlxnD1} are distributed across the entire dorsal neocortex (Fig, 1a, Matho 2021). Therefore, *Fezf2*- and *PlxnD1*- driver lines represent specific and reliable tools that categorically distinguish the top-level PT and IT classes.

Distinct cortical activation patterns of IT^{PlxnD1} and PT^{Fezf2} during quiescent resting state and spontaneous movements

To examine IT^{PlxnD1} and PT^{Fezf2} activation patterns reflected by their calcium dynamics, we bred *PlxnD1* and *Fezf2* driver lines with a Cre-activated GCaMP6f reporter line (Ai148). Using serial two-photon tomography (STP), we revealed global GCaMP6f expression pattern for each cell type across the dorsal cortex. Consistent with previous results [31], GCaMP6f expression was restricted to L2/3 and 5a PyNs in *PlxnD1* mice, and to L5b and to a lower extent in L6 PyNs in *Fezf2* mice (Fig. 1a.). We first characterized network dynamics of IT^{PlxnD1} and PT^{Fezf2} during wakeful resting state in head-fixed mice using epifluorescence wide-field imaging to measure neuronal activity across the dorsal cortex (Extended data1a, b). During this state, animals alternated between quiescence and spontaneous whisker, forelimb, and orofacial movements (Suppl. Videos 1, 2). We quantified full frame variance from behavioral videos recorded simultaneously with wide-field GCaMP6f imaging and identified episodes of quiescence and movements (active, Fig. 1c, methods). We measured standard deviations of neural activity for all pixels in each episode and found significantly higher activity during spontaneous movements versus quiescent episode in both cell types (Extended data 2b; IT^{PlxnD1} Quiescent Vs. Active Std. Dev. median (1st–3rd quartile), 0.0082 (0.008 – 0.0085) Vs. 0.01 (0.0085 – 0.0114); PT^{Fezf2} Quiescent Vs. Active, 0.0057 (0.0052 – 0.0067) Vs. 0.0077 (0.0068 – 0.0128)). We then measured the peak normalized variance per pixel to obtain a cortical activation map during each episode. While both IT^{PlxnD1} and PT^{Fezf2} were active across broad areas, they differed significantly in strongly active areas (Fig. 1d, Extended data 2a). In quiescent episodes, IT^{PlxnD1} were most active across forelimb, hindlimb, and frontolateral regions while PT^{Fezf2} were strongly active in posteromedial parietal areas. During spontaneous movement episodes, IT^{PlxnD1} showed strong activation in hindlimb and visual sensory areas while PT^{Fezf2} showed localized activation in the posteromedial parietal regions, with lower activation in other regions (Fig. 1d, Extended data 2a). To measure consistency of resting state activity patterns we quantified Pearson's correlation between spatial maps across mice and session and found strong correlation within and weak correlation between PN types (Extended data 2c; $IT^{PlxnD1\ Vs.\ PlxnD1}$ Vs. $PT^{Fezf2\ Vs.\ Fezf2}$ Vs. IT/$PT^{PlxnD1\ Vs.\ Fezf2}$ correlation coefficient (r) median (1st – 3rd quartile), 0.65 (0.52 - 0.74) Vs. 0.64 (0.53 – 0.71) Vs. 0.22 (0.09 – 0.47)) during quiescent episodes. During spontaneous movement (Active) episodes, IT^{PlxnD1} activity maps were far more variable compared to PT^{Fezf2} (Extended data 2d; $IT^{PlxnD1\ Vs.\ PlxnD1}$ Vs. $PT^{Fezf2\ Vs.\ Fezf2}$ Vs. IT/$PT^{PlxnD1\ Vs.\ Fezf2}$ correlation coefficient (r) median (1st – 3rd quartile), 0.44 (0.31 – 0.58) Vs. 0.81 (0.77 – 0.86) Vs. 0.39 (0.18 – 0.55)). Principal component analysis on the combined spatial maps of both PyN types revealed non-overlapping clusters across both episodes, indicating distinct cortical activation patterns between IT^{PlxnD1} and PT^{Fezf2} (Extended data 2f,g).

To investigate the correlation between neural activity and spontaneous movements, we built a linear encoding model using the top 200 singular value decomposition (SVD) temporal components of the behavior video as independent variables to explain the top 200 SVD temporal components of cortical activity dynamics (Extended data 3a, b). By measuring the proportion of 5-fold cross-validated activity variance explained by spontaneous movements (Methods), we found PT^{Fezf2} activity to be more strongly associated with spontaneous movements compared to IT^{PlxnD1} (Fig. 1e; IT^{PlxnD1} vs. PT^{Fezf2} cvR^2 (%) median (1st–3rd quartile), 23.7 (16.8 – 30) vs. 35.6 (28.2 – 46.1); Methods). We then extracted

mean time varying variance from parts of the behavior video frames covering nose, mouth, whisker, and forelimb regions (Fig. 1f inset) and identified the proportion of neural variance accounted by each body movement (Extended data 3c). While whisker and mouth contributed to some extent and equally between the two PyN types, forelimbs contributed significantly larger fraction of neural activity of PT^{Fezf2} than IT^{PlxnD1} (Fig. 1f; IT^{PlxnD1} Vs. PT^{Fezf2} cvR^2 (%) median (1st–3rd quartile), whiskers 10 (7.9 – 13.4) Vs. 13.4 (10 – 14.9), nose 5.8 (2.8 - 7.7) Vs. 4.8 (-1.1 – 8.3), mouth 8.5 (7.5 – 13.3) Vs. 12.6 (10 – 17.1), forelimbs 11.5 (7.5 – 16.4) Vs. 19.9 (13.8 – 17.3); Methods). We transformed the forelimb regression weights to the spatial domain of the neural activity (Methods) and found parietal region to be most active in PT^{Fezf2} while IT^{PlxnD1} was active within forelimb-hindlimb sensory areas (Suppl. Fig 2e). Together, these results demonstrate distinct activation patterns of IT^{PlxnD1} and PT^{Fezf2} during wakeful resting state, and preferential PT^{Fezf2} activation in parietal cortex associated with spontaneous movements compared to IT^{PlxnD1}.

Unimodal sensory inputs preferentially activate IT^{PlxnD1} over PT^{Fezf2}

We next investigated IT^{PlxnD1} and PT^{Fezf2} activation following sensory inputs of the somatosensory and visual system (Fig. 1g, Methods). We computed mean responses across time for the stimulus duration associated with whisker, orofacial and visual stimulation to identify activated cortical areas (Fig. 1h.). Light stimulation and tactile stimulation of whisker and orofacial region strongly activated IT^{PlxnD1} in primary visual, whisker and mouth-nose somatosensory cortex but resulted in no or weak activation of PT^{Fezf2} in those cortical areas (Fig 1h). To compare response intensities, we identified centers of maximum activation from the IT^{PlxnD1} spatial maps and extracted temporal signals within a circular window around the centers and computed single trial dynamics and trial averaged responses from both PyN types (Fig. 1i-k). Again, we found strong IT^{PlxnD1} activation but weak PT^{Fezf2} activation in primary sensory cortices in response to whisker, orofacial, and visual stimulus (Fig. 1j,k). We then measured response intensities by integrating the signal for the stimulus duration and found significantly higher activity in IT^{PlxnD1} compared to PT^{Fezf2} (Fig. 1l; IT^{PlxnD1} Vs. PT^{Fezf2} AUC (au) median (1st – 3rd quartile), whisker stimulation 0.045 (0.037-0.054) Vs. 0.007 (0.003 – 0.01), orofacial stimulation 0.035 (0.026 – 0.044) Vs. 0.003 (0 – 0.008), visual stimulation 0.033 (0.02 – 0.077) Vs. 0.008 (0.003 – 0.013)). To visualize sensory responses across cortical regions irrespective of response intensity, we peak normalized the maps and found activation in corresponding sensory cortices in PT^{Fezf2} along with broader activation including the retrosplenial areas (Extended data 4a). We measured consistency in activation patterns by computing the Pearson's correlation between the spatial maps across mice and sessions and found stronger correlations between IT^{PlxnD1} spatial maps compared to PT^{Fezf2} (Extended data 4b; $IT^{PlxnD1\ Vs.\ PlxnD1}$ Vs. $PT^{Fezf2\ Vs.\ Fezf2}$ Vs. $IT/PT^{PlxnD1\ Vs.\ Fezf2}$ correlation coefficient (r) median (1st – 3rd quartile), whisker stimulation 0.77 (0.73 – 0.82) Vs. 0.49 (0.26 – 0.59) Vs. 0.37 (0.22 – 0.54), orofacial stimulation 0.86 (0.8 – 0.89) Vs. 0.31 (0.05 – 0.57) Vs. 0.50 (0.24 – 0.99), visual stimulation 0.84 (0.8 – 0.87) Vs. 0.56 (0.40 – 0.71) Vs. 0.63 (0.55 – 0.71)). To confirm that difference in response was not due to a generally lower GCaMP6f signal (Signal to Noise Ratio) in PT^{Fezf2} we compared distribution of df/f values during spontaneous behavior and found that both PNs show df/f values across a similar range (Extended data 4c). Moreover, even during feeding behavior described later, both PNs express df/f values across comparable range. These results provide the first set of in vivo evidence that sensory inputs predominantly activate IT compared to PT PNs and that IT activation per se does not

lead to significant PT activation at the population level. These results are consistent with previous findings that thalamic input predominantly impinges on IT but not PT cells [32]. Surprisingly, IT activation per se does not lead to significant PT activation, despite demonstrated synaptic connectivity from in vitro studies [33].

Distinct PT^{Fezf2} and IT^{PlxnD1} subnetworks tuned to different sensorimotor components of a feeding behavior

To examine the activation patterns of IT^{PlxnD1} and PT^{Fezf2} during sensorimotor processing, we designed a head-fixed setup that captures several features of naturalistic mouse feeding behavior. In this setup, mice sense a food pellet approaching from the right side on a moving belt, retrieve pellet into mouth by licking, recruit both hands to hold the pellet and then initiate repeated bouts of hand-mouth coordinated eating movements that include: bite while handling the pellet, transfer pellet to hands while chewing, raise hands to bring pellet to mouth thereby starting the next bout (Fig. 2a, Suppl video 3). We used DeepLabCut [34] to track pellet and body parts in video recordings and wrote custom algorithms to identify and annotate major events in successive phases of this behavior (Methods, Fig. 2b, Extended data 5a, Suppl. Video 3).

We then imaged the spatiotemporal activation patterns of IT^{PlxnD1} and PT^{Fezf2} across dorsal cortex while mice engage in the behavior (Suppl. Videos 4, 5). We calculated average GCaMP6f signals per pixel in frames taken at multiple time points centered around when mice retrieve pellet into the mouth (pellet-in-mouth, or PIM) (Fig. 2c, frames displayed at 200ms time steps). Upon sensing the pellet approaching from the right side, mice adjust their postures and limb grips of the supporting hand bar while initiating multiple right-directed licks until retrieving the pellet into the mouth. During this period (Fig.2c, -0.7-0 seconds), IT^{PlxnD1} was first activated in left whisker primary sensory cortex (SS_{bfd}), which then spread to bi-lateral forelimb and hindlimb sensory areas (Fig 2c, Suppl. Video 4). Almost simultaneously or immediately after, PT^{Fezf2} was strongly activated in left medial parietal cortex (parietal node) just prior to right-directed licks, followed by bi-lateral activation in frontal cortex (medial secondary motor cortex, frontal node) during lick and pellet retrieval into mouth (Fig 2c, Suppl. Video 5). During the brief PIM period when mice again adjusted postures and then lift both hands to hold the pellet (Fig 2c, 0-0.1 sec), IT^{PlxnD1} was activated in bi-lateral orofacial primary sensory cortex (frontolateral posterior node; FLP) and subsequently in an anterior region spanning the lateral primary and secondary motor cortex (frontolateral anterior node; FLA), while PT^{Fezf2} activation shifted from bi-lateral frontal to parietal node. In particular, PT^{Fezf2} activation in parietal cortex reliably preceded hand lift. Following initiation of repeated bouts of eating actions, IT^{PlxnD1} was prominently activated in bilateral FLA and FLP specifically during coordinated oral-manual movements such as biting and handling, whereas PT^{Fezf2} activation remained minimum throughout the dorsal cortex. Notably, both IT^{PlxnD1} and PT^{Fezf2} showed much reduced activation during chewing. Since major components of the behavior task were lateralized towards the right side upon arrival of food pellet, we measured normalized direction of licking relative to the nose. Mice from both cell types predominantly licked towards the right side to pick the arriving pellet as soon as it was within reach of the tongue (Extended data 5b). To further investigate if one hemisphere was significantly more active than the other, we measured mean difference in activity between both hemispheres during the feeding sequence

(Methods). IT^{PlxnD1} showed stronger activity in the left hemisphere around barrel cortex presumably associated with sensing the pellet with its right whiskers while PT^{Fezf2} was also more active in the left hemisphere but around the parietal and frontal node possibly associated with preferential licking to the right together with other whole body movements (Extended data 5b,c).

To obtain a spatial map of cortical activation during specific feeding events, we build a linear encoding model using binary time stamps associated with the duration of lick, PIM, hand lift, handling, and chewing as independent variables to explain the top 200 SVD temporal components of neural activity. We then transformed the regression weights obtained from the model to the spatial domain of neural activity using SVD spatial components to obtain a cortical map of weights associated with each event (Fig. 2d, Methods). This analysis largely confirmed and substantiated our initial observations (Fig. 2c). Indeed, during lick onset IT^{PlxnD1} was active in left barrel cortex and bilateral forelimb/hindlimb sensory areas, which correlated with sensing the approaching pellet with contralateral whiskers and limb adjustments, respectively. In sharp contrast, PT^{Fezf2} was active along a medial parietal-frontal axis, which correlated with licking. During PIM, IT^{PlxnD1} was preferentially active in FLP with lower activity in FLA as well as in forelimb/hindlimb sensory areas, while PT^{Fezf2} was still active along the parietofrontal regions. Prior to and during hand lift, PT^{Fezf2} showed strong activation specifically in bilateral parietal areas, whereas IT^{PlxnD1} showed predominant bilateral activation in both FLA and FLP. During eating and pellet handling, IT^{PlxnD1} was strongly active in FLA and less active in FLP, while PT^{Fezf2} was only weakly active specifically in the frontal node (Fig 2d, note scale change in panels). Both IT^{PlxnD1} and PT^{Fezf2} showed significantly reduced activity across dorsal cortex during chewing (Fig. 2d).

To capture the most prominently activated cortical areas associated with key events of the behavior, we computed average activity per pixel during the progression from licking, retrieving pellet into mouth, to hand lift across mice and sessions (from 1 second before to 2 seconds after PIM). This analysis confirmed that, while both cell types were activated across multiple regions, PT^{Fezf2} activation was most prominent along a medial parietal-frontal network whereas IT^{PlxnD1} was most strongly engaged along a frontolateral FLA-FLP network (Fig. 3a,d). To characterize the temporal activation patterns of these key cortical nodes during behavior, we extracted temporal traces from the center within each of these 4 areas (averaged across pixels within a 280 µm radius circular window) and examined their temporal dynamics aligned to the onset of lick, PIM, and hand lift (Fig 3b,c,e,f). PT^{Fezf2} activity in the frontal node rose sharply prior to lick, sustained for the duration of licking until PIM, then declined prior to hand lift; on the other hand, PT^{Fezf2} activity in the parietal node increased prior to lick then declined immediately after, followed by another sharp increase prior to hand lift then declined again right after. In contrast, IT^{PlxnD1} activities in FLA and FLP did not modulate significantly during either licking or hand lift but increased specifically only when mice first retrieved pellet into mouth; while activation in FLP decreased following a sharp rise after pellet-in-mouth, activities in FLA sustained during biting and handling (Fig. 3g,i).

To examine more precise temporal relationship between the activation of these nodes, we measured the peak rate of change of signals (first derivative) centered to PIM for IT^{PlxnD1} and lick onset for PT^{Fezf2}

(Extended data 6a). IT^{PlxnD1} activities in FLP showed a steeper increase compared to FLA while PT^{Fezf2} activities in parietal node rose more sharply compared to the frontal node. These results suggest that FLP was activated prior to FLA within IT^{PlxnD1} and parietal node was activated prior to frontal within PT^{Fezf2} (Fig. 3h,j, Extended data 6a; PT^{Fezf2} Parietal Vs. Frontal peak rate of change (au) median (1st – 3rd quartile), 0.16 (0.13 – 0.21) Vs. 0.12 (0.1 – 0.16), IT^{PlxnD1} FLP Vs. FLA peak rate of change (au), 0.09 (0.06 – 0.12) Vs 0.07 (0.05 - 0.1)). To examine cortical dynamics from both populations within the same region, we measured GCaMP6f signals centered to PIM from all four nodes for each cell type. PT^{Fezf2} showed strong activation within parietal and frontal nodes specifically during lick and hand lift, whereas IT^{PlxnD1} showed significantly lower activation within these nodes during these episodes (Fig. 3k,l). In sharp contrast, IT^{PlxnD1} was preferentially active in FLA and FLP specifically during PIM with sustained activity especially in FLA during biting and handling, but no associated activity was observed in PT^{Fezf2} within these nodes during the same period (Fig. 3k,l).

To validate the differential temporal dynamics between PN types we performed linear discriminant analysis (LDA) on combined single trials of IT^{PlxnD1} and PT^{Fezf2} in each node (Methods). We trained an LDA model to discriminate if single trial activity from a node was associated with either IT^{PlxnD1} or PT^{Fezf2} and projected traces onto the top two dimensions identified by LDA to visualize the spatial distribution of projected clusters. This analysis revealed that IT^{PlxnD1} and PT^{Fezf2} activity clustered independently with little overlap, indicating that these PNs follow distinct temporal dynamics within each region (Fig. 3m).
Altogether, these results indicate that IT^{PlxnD1} and PT^{Fezf2} operate in distinct and partially parallel cortical subnetworks, which are differentially engaged during specific sensorimotor components of an ethologically relevant behavior.

Feeding without hand occludes parietal PT^{Fezf2} activity

To investigate if the observed PN neural dynamics were causally related to features of the feeding behavior, we developed a variant of the feeding task in which mice lick to retrieve food pellet but eat without using hands (Fig. 4a); this was achieved by using a blocking plate to prevent hand lift until mice no longer attempted to use their hands during eating. We then measured IT^{PlxnD1}activity in FLA-FLP nodes and PT^{Fezf2} activities in parietal-frontal nodes aligned to the onset of lick and PIM, and compared activity dynamics to those during normal trials in the same mice when they used hands to eat (Fig. 4b-e, Extended data 7a,b). Whereas PT^{Fezf2} activity in the frontal node did not show a difference with or without hand lift (Fig 4c, Extended data 7a, b), PT^{Fezf2} activity in parietal node showed a significant decrease in trials without hand lift specifically during the time when mice would have lifted hand during normal feeding trials (Fig 4c, Extended data 7a, b). On the other hand, IT^{PlxnD1} activity in FLA and FLP did not change for the duration from retrieving pellet through hand lift in trials with no hand lift compared with those in normal trials with hand lift. However, IT^{PlxnD1} activities in FLA and FLP showed a notable reduction during the eating-handling phase (Fig. 4d,e, Extended data 7a,b). We then computed integral of activity from PIM onset to 1 second after and compared results between trials with and without hand lift. Only PT^{Fezf2} activities in parietal node showed a sharp decline whereas IT^{PlxnD1} activities across FLA and FLP did not change significantly during the hand lift phase (Fig. 4f,g; PT^{Fezf2} Parietal lift Vs. no lift activity intensity (au) median (1st – 3rd quartile), 0.023 (0.017 – 0.03) Vs.

0.014 (0.008 – 0.019), PT^{Fezf2} Frontal lift Vs. no lift, 0.018 (0.013 – 0.023) Vs. 0.018 (0.014 – 0.022), IT^{PlxnD1} FLP lift Vs. no lift 0.013 (0.01 – 0.017) Vs. 0.013 (0.009 – 0.019), IT^{PlxnD1} FLA lift Vs. no lift 0.014 (0.01 – 0.018) Vs. 0.015 (0.012 – 0.019)).

To visualize cortical regions differentially modulated between feeding trials with or without hand-lift, we computed mean pixel-wise activity during a 1 second period after PIM onset from both trial types and subtracted the spatial map of no-hand-lift trials from that of hand-lift trials. As expected parietal activity was much higher in PT^{Fezf2} during hand-lift compared to no-hand-lift trials (Fig. 4h,i). These results reveal a causal link between parietal PT^{Fezf2} activation and hand lift movement during feeding; they also suggest that IT^{PlxnD1} activity in FLA and FLP is in part related to sensorimotor components of mouth feeding actions.

Inhibition of parietofrontal and frontolateral subnetworks differentially disrupts sensorimotor components of feeding behavior

To investigate the causal contribution of parietofrontal and frontolateral networks in pellet feeding behavior, we adopted a laser scanning method to optogenetically inhibit bilateral regions of dorsal cortex using vGat-ChR2 mice expressing Channelrhodopsin-2 in GABAergic inhibitory neurons (Fig. 5a). We examined the effects of bilateral inhibition of parietal, frontal, FLP and FLA nodes on different components of the behavior including pellet retrieval by licking, hand lift after PIM, and mouth-hand mediated eating bouts. We pooled the data from FLA and FLP as we did not observe major differences in disrupting each of the two areas.

During the pellet retrieval phase, inhibition of frontal and the frontolateral nodes prior to lick onset resulted in a sharp decrease of tongue extension, which recovered on average after about 0.5 seconds (Fig. 5b,c, Suppl. Video 6, before Vs. during inhibition tongue length (au) median (1st – 3rd quartile), frontal 6.52 (0 – 10.08) Vs. 4.54 (1.1 – 6.85), parietal 8.95 (1.47 – 13.37) Vs. 7.65 (4.25 – 10.79), frontolateral 3.89 (0 – 9.15) Vs. 1.4 (0 – 3.6)); inhibition also led to a significant delay and disruption in pellet retrieval to mouth (Fig. 5d; control Vs. inhibition pim onset time (sec) median (1st – 3rd quartile), frontal 4.81 (4.66 – 5.12) Vs. 5.07 (4.82 – 5.85), parietal 4.79 (4.66 – 5.13) Vs. 4.93 (4.66 – 5.26), frontolateral 4.77 (4.56 – 5.12) Vs. 5.07 (4.61 – 10.96)). These effects were not observed when inhibiting the parietal node (Fig. 5b-d). During the hand-lift phase after PIM, inhibition of frontal and frontolateral nodes prior to hand lift onset led to substantial deficit in the ability to lift hands towards mouth, resulting in a sharp decrease in the number of hand lift (Fig. 5e, Suppl. Video 7); notably, in trials when animals did initiate hand lift despite inhibition, hand trajectories appeared smooth and normal. Upon inhibiting the parietal node, on the other hand, no significant decrease of hand lift numbers per se was observed but there were substantial deficits in hand lift trajectory, characterized by erratic and jerky movements (Fig. 5f, Suppl. Video 8). To quantify these deficits, we measured the absolute value of the first derivative of 15 Hz low pass filtered hand lift trajectory to obtain the time varying velocity during the lift episode and compared its integral between 0 to 1 second after hand lift between inhibition and control trials. While frontal and frontolateral inhibition did not affect lift trajectories among the successful trials, parietal inhibition resulted in a significant modulation of velocity during lift, indicating deficits in coordinating hand movements (Fig. 5f,g; control Vs.

inhibition area under curve (au) median (1st – 3rd quartile), frontal 1.36 (1.02 – 1.69) Vs. 1.29 (0.87 – 1.68), parietal 1.34 (1.11 – 1.79) Vs. 1.78 (1.25 – 2.35), frontolateral 1.39 (1.1 – 1.59) Vs. 1.43 (1.12 – 1.77)).

During eating bouts with coordinated mouth-hand movements, after the initial hand lift from support bar to hold pellet in mouth, inhibiting the frontal and frontolateral nodes severely impeded mice's ability to bring pellet to mouth (i.e. secondary hand lifts when mice bring pellet to mouth after holding it while chewing); this deficit recovered immediately after the release of inhibition (Suppl. Video 9). Inhibiting the parietal node resulted in only a slight disruption of these secondary hand lifts (Fig. 5h). To quantify these deficits, we measured the average distance of left fingers to the mouth, number of secondary hand lifts, and the duration of the hand held close to mouth. We found significant deficits in all these parameters in inhibition trials for all four cortical areas compared to those of control trials (Fig. 5i-k; control Vs. inhibition finger-mouth distance (au) median (1st – 3rd quartile), frontal 0.15 (0.13 – 0.17) Vs 0.18 (0.16 – 0.21), parietal 0.14 (0.11 – 0.18) Vs. 0.16 (0.13 – 0.19), frontolateral 0.14 (0.11 – 0.17) Vs. 0.2 (0.17 – 0.23), control Vs. inhibition number of secondary handlifts median (1st – 3rd quartile), frontal 2 (1 - 3) Vs. 1 (0 - 1), parietal 2 (1 – 3) Vs. 1 (1 – 2), frontolateral 3 (2 – 3.25) Vs. 1 (0 – 2), control Vs. inhibition hand at mouth duration (sec) median (1st – 3rd quartile), frontal 1.85 (1.44 – 2.27) Vs. 1.07 (0.44 – 1.27), parietal 1.74 (1.27 – 2.2) Vs 1.48 (0.93 – 1.93), frontolateral 2.25 (1.76 – 2.59) Vs. 1.22 (0.83 – 1.66)). These results suggest that the parietofrontal and frontolateral networks differentially contribute to orchestrating orofacial and forelimb movements that enable pellet retrieval and mouth-hand coordinated eating behavior. Considering the spatiotemporal activation patterns of PT^{Fezf2} and IT^{PlxnD1} during this behavior (Fig. 2, 3), it is likely that PT^{Fezf2} might mainly contribute to the function of parietofrontal network and IT^{PlxnD1} might mainly contribute to function of frontolateral network.

Distinct projection patterns of IT^{PlxnD1} frontolateral and PT^{Fezf2} parietofrontal subnetworks

To explore the anatomical basis and IT^{PlxnD1} and PT^{Fezf2} subnetworks revealed by wide-field calcium imaging, we examined their projection patterns by anterograde tracing using recombinase-dependent AAV in driver mouse lines. Using serial two photon tomography (STP) across the whole mouse brain [35], we extracted the brain wide axonal projections and registered them to the Allen mouse Common Coordinate Framework (CCFv3, Methods, [36,37]). Using 3D masks generated from the CCF-registered map for each brain, we quantified and projected axonal traces within specific regions across multiple planes. With an isocortex mask, we extracted axonal traces specifically within the neocortex and projected signals to the dorsal cortical surface (Fig. 6a).

As expected, PT^{Fezf2} in parietal and frontal region show very little intracortical projections (Fig 6a, Extended data 8a, Suppl. Videos 12,13), thus we focused on characterizing their subcortical targets (Fig. 6b, Extended data 8b-e, Suppl. Videos 12,13). PT^{Fezf2} in frontal node predominantly project to dorsal striatum, pallidum (PAL), sensorimotor and polymodal thalamus (THsm, THpm), hypothalamus (HY), motor and behavior state related midbrain regions (MBmot, MBsat), and motor and behavior state related Pons within the hindbrain (P-mot, P-sat, Fig 6b, Extended data 8b-e). PT^{Fezf2} in parietal node projected to a similar set of subcortical regions as those of frontal node, but often at

topographically different locations within each target region (Fig. 6b, Extended data 8b-e). To analyze the projection patterns, we projected axonal traces within the 3D masks for each regions across its coronal and sagittal plane. For example, PT^{Fezf2} in parietal and frontal nodes both projected to the medial regions of caudate putamen (CP), with frontal node to ventromedial region and parietal node to dorsomedial regions (Extended data 8b); they did not project to ventral striatum. Within the thalamus, frontal PT^{Fezf2} project predominantly to ventromedial regions both in primary and association thalamus while parietal PT^{Fezf2} preferentially targeted dorsolateral regions in both subregions (Extended data 8c). Within the midbrain, we mainly examined projections across collicular regions and found that frontal and parietal PT^{Fezf2} specifically targeted the motor superior colliculus (SCm) with no projections to sensory superior colliculus or inferior colliculus. Within SCm, frontal PT^{Fezf2} preferentially targeted ventrolateral regions while parietal PT^{Fezf2} projected to dorsomedial areas (Extended data 8d). Together, the large set of PT^{Fezf2} subcortical targets may mediate the intention, preparation, and coordinate the execution of tongue and forelimb movements during pellet retrieval and handling. In particular, the thalamic targets of parietofrontal nodes might project back to corresponding cortical regions and support PT^{Fezf2}-mediated cortico-thalamic-cortical pathways, including parietal-frontal communications.

In contrast to PT^{Fezf2}, IT^{PlxnD1} formed extensive projections within cerebral cortex and striatum (Fig. 6b, Extended data 8b, Suppl. Videos 10,11). Within the dorsal cortex, IT^{PlxnD1} in FLA projected strongly to FLP and to contralateral FLA, and IT^{PlxnD1} in FLP projected strongly to FLA and to contralateral FLP. Therefore, IT^{PlxnD1} mediate reciprocal connections between ipsilateral FLA-FLP and between bilateral homotypic FLA and FLP (Fig. 6a). In addition, IT^{PlxnD1} from FLA predominantly project to FLP (MOp), lateral secondary motor cortex (MOs), forelimb and nose primary sensory cortex (SSp-n, SSp-ul), secondary sensory cortex (SSs) and visceral areas (VISC). Interestingly, IT^{PlxnD1} in FLP also project to other similar regions targeted by FLA (Fig. 6b). Beyond cortex, IT^{PlxnD1} in FLA and FLP projected strongly to the ventrolateral and mediolateral division of the striatum, respectively (STRd, Fig. 6b, Extended data 8b). These reciprocal connections between FLA and FLP and their projections to other cortical and striatal targets likely contribute to the concerted activation of bilateral FLA-FLP subnetwork during pellet eating bouts involving coordinated mouth-hand sensorimotor actions. Therefore, as driver lines allow integrated physiological and anatomical analysis of the same PN types, our results begin to uncover the anatomical and connectional basis of functional IT^{PlxnD1} and PT^{Fezf2} subnetworks.

IT^{PlxnD1} and PT^{Fezf2} show distinct spatiotemporal dynamics and spectral properties under ketamine anesthesia

Given the distinct spatiotemporal activation patterns of IT^{PlxnD1} and PT^{Fezf2} in wakeful resting states and sensorimotor behaviors, we further explored whether they differ in network dynamics in a dissociation-like brain state under ketamine/xylazine anesthesia [29,38]. We first sampled the temporal activity patterns across 6 different regions of dorsal cortex and found that both cell types showed robust oscillatory activity, with IT^{PlxnD1} displaying faster dynamics than PT^{Fezf2} (Fig. 7a, Suppl. Videos 14,15). Quantification of the spectrograms and relative power spectral densities across cortical regions showed

that IT^{PlxnD1} exhibited oscillations at approximately 1-1.4 Hz while PT^{Fezf2} fluctuated at 0.6-0.9 Hz (Fig. 7b-d, Extended data 9a; IT^{PlxnD1} Vs. PT^{Fezf2} 0.6-0.9 Hz. relative power median (1st – 3rd quartile), MOp 0.0035 (0.0025 – 0.0038) Vs. 0.003 (0.002 – 0.0042), RSp 0.0022 (0.0016 – 0.0032) Vs. 0.0042 (0.0015 – 0.0063), IT^{PlxnD1} Vs. PT^{Fezf2} 1-1.4 Hz. relative power median (1st – 3rd quartile), MOp 0.0021 (0.0017 – 0.0029) Vs. 0.0009 (0.0006 – 0.0012), RSp 0.0041 (0.0031 – 0.0051) Vs. 0.0028 (0.0018 Vs. 0.0034)).

To visualize a map of cortical regions strongly oscillating at these frequencies, we computed a map of normalized averaged power between 0.6-0.9 and 1-1.4 Hz for each pixel (methods). While IT^{PlxnD1} was strongly active within the frontolateral and posterolateral regions, PT^{Fezf2} was predominantly active in the retrosplenial regions across both frequency bands (Fig. 7e, Extended data 9b). To determine distinct pattern of power distribution across mice and sessions, we performed PCA on these spatial maps and projected them onto the top two dimension for each frequency band (Extended data 9c). IT^{PlxnD1} and PT^{Fezf2} both clustered independently with further segregation between IT^{PlxnD1} 0.6-0.9 Hz and 1-1.4 Hz frequency bands (Extended data 9c). Furthermore, these two PN types manifested distinct spatial dynamics across the dorsal cortex, which was visualized by generating a space-time plot displaying activity from pixels obtained across a slice of the cortical surface (Methods, Fig. 7f). While IT^{PlxnD1} displayed complex spatiotemporal patterns with activities spreading, for example, from central regions to anterolateral and posteromedial or from posteromedial to anterolateral and back, PT^{Fezf2} activities predominantly originated from retrosplenial regions and spread to anterolateral regions (Fig. 7f, Suppl. Videos 14,15). To identify the most dominant spatial activation pattern, we performed seqNMF [39,40] on the activity data and found that the top dimension accounted for more than 80 % of the variance in IT^{PlxnD1} and over 90% in PT^{Fezf2}. Furthermore, we found significant differences in the spatial propagation of activities between the two cell types: whereas IT^{PlxnD1} activities spread multi-directions across most of the dorsal cortex, PT^{Fezf2} activities mainly propagated from retrosplenial toward the frontolateral regions (Fig. 7g, Extended data 9d). These results show that even under unconstrained brain state such as during anesthesia, IT^{PlxnD1} and PT^{Fezf2} subnetworks operate with distinct spatiotemporal dynamics and spectral properties, likely reflecting their differences in biophysical, physiological [41], and connectional (e.g. Fig 6) properties.

Discussion

The quest for the cellular basis of cerebral cortex architecture has been fueled by successive waves of technical advances over the past century. Whereas early cytoarchitectonic analyses of cell distribution patterns identified numerous cortical areas [42] and characteristic laminar organization across different areas [43,44], single cell physiological recording was key to reveal the vertical groupings of neuronal receptive field properties, though initially in anesthetized state [3,4]. Since its formulation, columnar configuration as the basic units of cortical organization has been a foundational concept that guided decades of research to unravel its cellular and circuitry underpinnings [5]; yet to date the anatomic basis as well as functional significance of “cortical columns” remain elusive and contentious [45-47]. Multi-cellular recordings and computational simulation of neural connectivity led to the hypothesis of a

"canonical circuit" template, which may perform similar operations common across cortical areas [6-8,48]; but the cellular basis of a "canonical circuit" and its relationship to global cortical networks remain unsolved and largely unexplored. An enduring challenge for understanding cortical architecture is its neuronal diversity and wiring complexity across levels and scales [10]. Meeting this challenge requires methods to monitor and interpret neural activity patterns across multiple layers and large swaths of cortical territory yet with cell type resolution in real time and in behaving animals. The increasing recognition of and experimental access to diverse neuron types, groups of cells with similar molecular, anatomical, and physiological properties, as neural circuit elements is facilitating contemporary explorations of cortical organization [11]. Here, we combine genetic targeting of major PN types with cortex-wide imaging of their spatiotemporal dynamics in behaving mice. We discovered that genetic and projection defined PN types contribute to distinct and partially parallel subnetworks of cortical processing during a range of brain states and sensorimotor behaviors. These results call for a major revision in our conception of cortical architecture substantially shaped by the concept of columnar organization [46]; they suggest that dynamic areal and PN type-specific subnetworks are a key feature of cortical functional architecture that integrates across nested levels from microcircuit components to global brain networks. It is possible that columnar information flow between IT and PT, and thus the functional integration of corresponding subnetworks, might be dynamically gated by inhibitory and modulatory mechanisms according to brain states and behavioral demand.

Although widefield calcium imaging in rodent cortex provide an opportunity to bridge cellular and cortex-wide measurement of neural activity [22], realizing the full potential of this approach relies on the ability to resolve distinct and biologically relevant neuronal subpopulations. To date, most if not all of these studies examined mixed population (e.g. those defined by Thy1 and Rbp4 transgenic lines) comprising different projection classes [27-30], thus have yet to compare distinct PN projection types and link anatomical connectivity with functional dynamics. We have recently established genetic tools for dissecting the hierarchical organization PyN subpopulations based on their molecular genetic programs [31]; these tools enable accessing biologically significant PyN subpopulations through their inherent developmental, anatomical and physiological properties. Among diverse PN types, IT and PT represent two major top-level classes that mediate intracortical processing and subcortical output channels, respectively. Decades of studies have demonstrated their distinct gene expression programs [12,49], developmental trajectories [50], morphological and connectivity features [33,41], physiological and biophysical properties [41], and functional specializations in specific cortical areas and behavior [51-53]. Here we demonstrate that IT^{PlxnD1} and PT^{Fezf2} operate in separate and partially parallel subnetworks during a range of brain states and sensorimotor behaviors. These results begin to extend the concept of major neuron types linking molecular, developmental, and anatomical features to systems and functional level distinctions. Reliable experimental access to these PN types will facilitate a multi-faceted analysis to integrate cross-level mechanistic explanations that elucidate the nested level of cortical circuit architecture.

Although GCaMP6f signals could derive from somatic as well as dendritic compartments of PNs, modeling and experimental studies have suggested that signals measured by widefield imaging from cortical surface largely originate from the depth of cell body layer [54]. Furthermore, GCaMP6f signals

are strongly associated with neuronal action potentials both at single cell resolution [55] and across cortical depth in a local region [30,56]. It is important to note that GCaMP6f signals have relatively slow temporal dynamics (hundreds of milliseconds); complementary methods with proper temporal resolution for spiking activities (e.g. targeted electrophysiological recordings [57] are necessary to decipher information flow and neural circuit operation.

Studies in primates and rodents have shown that the posterior parietal cortex (PPC) is a major associational hub that receives inputs from virtually all sensory modalities and frontal motor areas, and supports a variety of functions including sensorimotor transformation, decision making, and movement planning [58-60]. In particular, PPC subdivisions are strongly connected with frontal secondary motor cortex in a topographically organized manner [61,62], and this reciprocally connected network has been implicated in movement intension, planning, and the conversion of sensory information to motor commands [63]. The cellular basis of parietal-frontal network is not well understood [59,64]. Here we found that sequential and co-activation of parietal-frontal PT^{Fezf2} neurons are the most prominent and prevalent activity signatures that precede and correlate with tongue, forelimb, and other body part movements. During the hand-assisted pellet feeding task, training mice to eat without hands specifically occluded PT^{Fezf2} parietal activation that normally precedes hand lift. Furthermore, optogenetic inhibition of the frontal node disrupts licking and hand lift, while the same manipulation of the parietal node disrupts the trajectory and coordination of hand-to-mouth movements. Together, these results suggest PT^{Fezf2} as a key component of the parietal-frontal network implicated in sensorimotor transformation and action control. As PT^{Fezf2} neurons do not extend significant intracortical projections, their co-activation in the parietal-frontal network might result from coordinated presynaptic inputs from, for example, a set of IT PNs that communicate between the two areas, or from cortico-thalamic-cortical pathways [32,65,66] linking these two areas. Leveraging genetic tools, future PN type-based anterograde, retrograde, and trans-synaptic tracing will reveal the cell type basis of parietal-frontal network. Furthermore, as the topographic connections between parietal and fontal subdivisions appear to correlate with multiple sensory modalities and body axis [61,62,64], cellular resolution analysis using two-photon imaging and optogenetically targeted recordings may resolve these topographically organized circuits that mediate different forms of sensorimotor transformation and action control.

While IT^{PlxnD1} neurons show broad and complex activity patterns during several brain states and numerous episodes of sensorimotor behaviors, we discovered a prominent FLP-FLA subnetwork that correlates to a specific aspect of eating involving coordinated mouth and hand movements. Notably, this subnetwork manifest low activity during pellet retrieval and initial hand lift to mouth, when PT^{Fezf2} in the parietal-frontal subnetwork is strongly active, as well as during chewing. While FLP mostly comprises primary sensory areas of the orofacial and forelimb regions, FLP comprises primary and secondary motor areas of these same body parts. The prominent reciprocal IT^{PlxnD1} projections between these two areas and across bilateral FLP-FLA suggest a compelling anatomical basis underlying the concerted activity dynamics of this functional subnetwork. Furthermore, optogenetic inhibition of FLP-FLA resulted in deficits of pellet handling during eating. Together, these results suggest a significant role of the FLP-FLA subnetwork in the sensorimotor coordination of orofacial and forelimb movement

during feeding. Systematic cell type-based studies of FLP and FLA may reveal the neural circuit basis underlying oro-manual dexterity for food handling and eating behaviors.

Given the vast diversity of PN types, our focus on IT^{PlxnD1} and PT^{Fezf2} populations in the current study does not achieve a full description of cortical network operations. Indeed, top-level classes further include cortico-thalamic, near-projecting, and layer 6b populations [12]; and the IT class alone comprises diverse transcriptomic [12] and projection [17] types that mediate myriad cortical processing streams [67]. Although IT^{PlxnD1} represents a major subset, other IT subpopulations remain to be recognized and analyzed using similar approaches. It is possible, for example, that another IT type might feature a direct presynaptic connection to PT^{Fezf2} (e.g. [7,33] and share a more similar spatiotemporal activity pattern and closer relationship to the PT^{Fezf2} subnetwork. Future studies will leverage emerging genetic tools to more systematically examine additional sets of PN types and subpopulations, thereby achieving an increasingly more comprehensive view of functional cortical networks. The proper granularity of cell type targeting need to depend on the question being addressed and match the granularity of behavior and functional readout. Furthermore, simultaneous analysis of two or more PN types in the same animal will be particularly informative in revealing their functional interactions underlying cortical processing.

Acknowledgments
We thank Joshua Hatfield for performing STP imaging PN projections. We are grateful to Anne Churchland for the numerous discussions, and to Tatiana Engel and Yanliang Shi for discussions on data analysis. We thank Steve Lisberger, Lindsey Glickfeld for comments on the manuscript. This research was supported NIH grant U19MH114823-01 to Z.J.H. Z.J.H is also supported by a NIH Director's Pioneer Award 1DP1MH129954-01.

Contributions
Z.J.H. and H.M. conceived the project. H.M. built setups, performed experiments and analyzed data. Z.J.H. supervised the research. X.A. provided advice on the design of feeding behavior and on building feeding behavior setup, and provided mice. P.M. provided advice for analyzing neural data. H.K. performed STP viral injections and surgeries. S.Z. performed in situ imaging experiments. S.M. offered advice on building wide-field imaging setup. Z.J.H. and H.M wrote the manuscript.

Data Availability
All data will be made available upon reasonable request.

Code Availability
All code will be posted on an online public server prior to publication.

Note

While this manuscript was in preparation, the following preprint was posted in bioRxiv:
Musall, S., Sun, X.R., Mohan, H., An, X., Gluf, S., Drewes, R., Osten, P., Churchland, A.K. (2021)
Pyramidal cell types drive functionally distinct cortical activity patterns during decision-making.
https://www.biorxiv.org/content/10.1101/2021.09.27.461599v2.abstract

Methods

Animals

43 male and female mice were included as part of the study. To express GCaMP6f within specific projection neuron (PN) population, 14 *FezF2-CreER* and 16 *PlexinD1-CreER* knockin mouse lines generated in the lab were crossed with Ai148 (The Jackson Laboratory, Strain #030328), a GCaMP6f reporter line. 3 *VGAT-ChR2-EYFP* (The Jackson Laboratory, Strain #014548) that express the blue light activated opsin ChR2 in GABAergic interneuron population were used for optogentic manipulation. 6 *PlexinD1-CreER* and 4 *FezF2-CreER* crossed with a reporter line expressing LSL-Flp were used for viral expression of flp depended anterograde tracing. Expression of reporters were controlled via the intraperitoneal injection of tamoxifen (20mg/ml, dissolved in corn oil) between 1 to 2 months postnatal. All mouse colonies at Cold Spring Harbor Laboratory (CSHL) were maintained in accordance with husbandry protocols approved by the IACUC (Institutional Animal Care and Use Committee) and housed by gender in groups of 2 – 4 with access to food and water *ad libitum* and 12 hour light-dark cycle.

Surgical procedures

For widefield calcium imaging and optogenetic manipulation, adult mice older than 6 weeks were anesthetized by inhalation of isoflurane maintained between 1-2%. Ketoprofen (5 mg kg−1) was administered intraperitonially as analgesia before and after surgery, and lidocaine (2–4 mg kg−1) was applied subcutaneously under the scalp prior to surgery. Mice were mounted on a stereotaxic headframe (Kopf Instruments, 940 series or Leica Biosystems, Angle Two). An incision was made over the scalp to expose the dorsal surface of the skull and the skin pushed aside and fixed in position with tissue adhesive (Vetbond 3M). The surface was cleared using saline and an outer wall was created using dental cement (C&B Metabond, Parkell; Ortho-Jet, Lang Dental) keeping most of the skull exposed. A custom designed circular head plate was implanted using the dental cement to hold it in place. After cleaning the exposed skull thoroughly, a layer of cyanoacrylate (Zap-A-Gap CA+, Pacer Technology) was applied to clear the bone and provide a smooth surface to image calcium activity or for optogenetic stimulation [24]. For viral injections, we followed the same anesthesia procedure. Under anesthesia, an incision was made over the scalp, a small burr hole drilled in the skull and brain surface was exposed. A pulled glass pipette tip of 20–30 μm containing the viral suspension was lowered into the brain; a 300–400 nl volume was delivered at a rate of 30 nl min^{-1} using a Picospritzer (General Valve Corp); the pipette remained in place for 10 min preventing backflow, prior to retraction, after which the incision was closed with 5/0 nylon suture thread (Ethilon Nylon Suture, Ethicon) or Tissueglue (3M Vetbond), and mice were kept warm on a heating pad until complete recovery [31].

Viruses

For cell type specific anterograde tracing we injected 300-400nl of flp dependent viral tracer (AAV2/8-Cag-fDIO TVAeGFP, UNC Vector Core) in *FezF2-CreER;LSL-Flp* mice at either the frontal node (1.7-1.85mm Anterior, 0.7mm lateral, 1.25 mm ventral) or the parietal node (-1.79 to -1.91 mm posterior, 1.25 to 1.35 mm lateral, 0.3-0.7 mm ventral) and in *PlexinD1-CreER;LSL-Flp*

mice at either FLA (1.7 mm anterior, 2.25 mm lateral, 0.3-0.8 mm ventral) or FLP (0.3mm anterior, 3mm lateral, 0.4-0.8mm dorsal). Mice were between 7 to 12 weeks during viral injection.

Whole-brain STP tomography and image analysis

Whole brain STP imaging was performed as described earlier [35]. Briefly, perfused and post fixed brains of adult mice were embedded in 4% oxidized-agarose in 0.05 M PB, cross-linked in 0.2% sodium borohydrate solution (in 0.05 M sodium borate buffer, pH 9.0–9.5).The entire brain was imaged in coronal sections with a 20× Olympus XLUMPLFLN20XW lens (NA 1.0) on a TissueCyte 1000 (Tissuevision) with a Chameleon Ultrafast-2 Ti:Sapphire laser (Coherent) exciting EGFP at 910 nm. Whole-brain image sets were acquired at 0.875 µm x 0.875 µm sampled for 230-270 z sections with a 50 µm z step size. Images were collected by two PMTs (PMT, Hamamatsu, R3896), for signal and autofluorescent background, using a 560-nm dichroic mirror (Chroma, T560LPXR) and band-pass filters (Semrock FF01-680/SP-25). The image tiles were corrected to remove illumination artifacts along the edges and stitched as a grid sequence. Image processing was completed using ImageJ/FIJI and Adobe/Photoshop software with linear level and nonlinear curve adjustments applied only to entire images.

To extract axonal traces, we first used brainreg [37 36] to register whole brain data to 10 µm CCFv3 Allen map [68]. After registration, whole brain background images were linearly fit to the imaging channel and regressed out. Background corrected signals were z-scored and a threshold ranging 0.5 to 1.5 was manually set for each brain above which signal was binarized. Regions with noise in each frame was manually removed using ImageJ/FIJI. To extract volume and peak normalized projection maps (Fig. 6b), we subdivided the whole brain into 43 major nodes as classified by allen map tree and grouped all regions below that node as part of the parent node mask. We then extracted total axonal count within each roi mask using the binarized data, scaled by the total volume of each mask and normalized by peak value across all nodes. To obtain spatial distribution of axons, 3D masks from registered Allen map for each node was used to extract signal enclosed within the roi from binarized data. Average of the projections within mask either along the coronal or sagittal dimension was obtained to extract axonal distribution across each plane. Masks were also projected along these dimensions and the edges used to obtain the borders for each node (Extended data 8b-e). All STP imaging analysis was performed on python 3.

In Situ Hybridizaion

Probes were ordered from Molecular Instruments. Mouse brain was sliced into 50 µm thick slices after PFA perfusion fixation and sucrose protection. Hybridization chain reaction in situ was performed via free floating method in 24 well plate. First, brain slices were exposed to probe hybridization buffer with HCR Probe Set at 37ºC for 24 hours. Brain slices were washed with probe wash buffer, incubated with amplification buffer and amplified at 25ºC for 24 hours. On day 3, brain slices were washed, counter stained with DAPI and mounted. PlexinnD1 (546 nm), Fezf2 (546 nm) and Satb2 (647 nm) probes were used to examine overlaps between these markers.

Feeding behavior paradigm

We developed a novel behavior paradigm where in mice use an ethological behavioral sequence to capture, handle and feed on food pellets while being head fixed. 2 seconds after trial start, a food pellet (14, 20 or 45 mg, Dustless Precision pellet, F05684, F0071, F0021, Bio-Serv) is delivered on to a custom designed conveyer belt (B375-150XL, Servocity) with a small pellet holder (made of Velcro strap) from an automatic food pellet dispenser (80209-45, Lafayette Instruments) after which a servo motor (38335S, Servocity) maneuvers the conveyer belt to bring pellets close to the head fixed mouse. The mouse uses its tongue to pick food pellet to its mouth; lift its hand from a wooden shaft to hold, handle and bite a part of it; bring hands down clasping the remaining pellet; chew; swallow and bring the clasped pellet back towards mouth to continue feeding. At the end of 15 seconds after trial start, the conveyer belt rotates back to dispose of any pellet that was not picked and then moves back to starting position under the pellet dispenser. Layout of task associated temporal events with probability distribution of lick bout onset, pellet in mouth onset, handlift onset, first handling and chew event times are visualized (Extended data 5a).

We began to train mice at least two days after head bar implantation. All mice were older than 6 weeks when training was initiated. Mice were first food restricted so that they reach about 80 to 85% of their initial body weight with ad libitum access to water. During food restriction, mice are fed food pellets (those used in the task) weighing about 10 to 15% of their body weight everyday. During this period mice were habituated to the setup by head fixing them in increasing durations starting from 10 minutes to 30 minutes over 4 days. After habituation and reaching about 85% of their initial weight, we manually placed food pellets close to its mouth while being head fixed. In the beginning mice pick food with their tongue and try to chew without lifting hands. After a few trials, they begin to lift hands to hold the pellet after picking it with their tongue often within the same session or sometimes after a couple of sessions. Once mice become comfortable in lifting their hands after picking pellet, we begin to deliver the pellet close to mouse automatically by moving the conveyer belt from the pellet dispenser. Most mice learn to perform the task within a week of initiating training. In each session mice consumed about 20 to 80 pellets depending on their body weight and days from onset of training. As days progress, mice tend to eat more pellets. At the end of every session, irrespective of the quantity they consume during the task, we provide food pellets weighing about 10 to 15% of their body weight. We constantly measure the mouse weight and make sure they are always above 85% of their initial weight. As sessions progress, they perform increasing number of trails even if their weight is at 90 % of initial body weight.

Behavior tracking and classification

Using two high speed cameras (FL3-U3-13S2C-CS, Teledyne FLIR) fitted with varifocal lens (#COT10Z0513CS, B&H), we recorded behavior from both the front and left side of the mouse at 100 frames per second as they performed the task under UV illumination. We used deeplabcut [34] to track a range of task components and body parts from both angles including the pellet, pellet holder, left wrist, lower lip, upperlip, nose, tongue tip, left three fingers and right three fingers (from front view). We developed custom algorithms that use these tracked features to identify and classify different behavior events. To identify onset of lick bouts, we calculated spectrogram of the tongue trajectory and extracted the time varying mean power between 4 to 10 Hz. Using a predefined threshold, we obtained time stamps associated with power rising above threshold and falling below it

to obtain the onset and offset times of a lick bout. The onset time of the first lick bout after pellet is delivered to the pellet holder was considered as the lick onset time. The time point when food pellet first crossed the lower lip, after being picked by the tongue, for at least 100 ms was considered as the pellet in mouth onset time. To identify handlift onset, we used left hand trajectory to detect time point when absolute velocity crossed a predefined threshold. To extract episodes of food handling, we built a long short term memory (LSTM) neural network classifier with 100 hidden units using MATLAB neural network tool box. After manually labelling time stamps associated with food handling for a few example trials across mice, we used these binary time stamps as output variable and all z-scored trajectories from front view (including the left three fingers, right three fingers, tongue, pellet, upperlip and lowerlip trajectories) of mice as input variables to train the classifier. We then used this classifier to extract time stamps associated with food handling for the remaining trials. To extract chew episodes, we computed spectrogram of the lower lip trajectory to obtain mean power between 3 to 8 Hz and used 0.05 times the standard deviation of this signal as the threshold above which events were classified as chewing. Only episodes longer than 0.5 seconds were used.

Wide-field calcium imaging

We used wide field imaging to simultaneously measure GCaMP6f activity across the dorsal cortex. The imaging system used was as described previously [24]. Briefly, we used a sCMOS (edge 5.5, PCO) camera in combination with a 105 mm focal length top lens (DC-Nikkor, Nikon) and 85 mm (85M-S, Rokinon) bottom lens resulting in a x1.24 magnification and a field of view of about 12.5 x 10.5 mm^2 with an image resolution of 640 x 540 pixels (about 20 µm per pixel dimension) after 4x spatial binning. Images were acquired at 60 Hz alternating between blue (470 nm collimated LED, M470L3, Thorlabs) and violet (405 nm collimated LED, M405L3, Thorlabs) excitation through the same excitation path with the help of a dichroic mirror (no. 87–063, Edmund optics) between the two paths and a 495 nm long pass dichroic (T495lpxr, Chroma) to project both LEDs onto cortical surface. A 525 nm band-pass filter (no. 86–963, Edmund optics) was placed between the camera and lenses to filter GCaMP emission signal. We used the signal associated with 405 nm excitation to regress out the non-calcium dependent hemodynamic signal and isolate the true calcium dependent signal from the 470 nm excitation as described previously (Allen et al., 2017). For each pixel, 405 nm and 470 nm excited signals were first ΔF/F normalized using the median across time series within a trial. Signal associated with 405 nm excitation was filtered with a 330 msec (10 frames) moving average filter and linearly fit to the 470 nm excitation signal to obtain regression coefficients. The raw 405 nm excited signal was scaled using these coefficients and regressed out from the 470 nm excited signal to obtain calcium depended ΔF/F signal. For spontaneous and ketamine anesthetized measurements, since activity was measured for 180 seconds continuously, signal was first detrended by fitting and subtracting a 7th order polynomial to the raw signal associated with 405 nm and 470 nm excitation (Extended data 1c) prior to regressing out non-calcium dependent signal as described before. This resulting imaging rate of 30 frames per second after hemodynamic correction was used for all subsequent analysis of calcium activity. All widefield data were rigidly aligned to the Allen CCFv3 dorsal map using four anatomical landmarks; the left, center and right edges of the anterior ridge between the frontal cortex and the olfactory bulb and the lambda [24,68] there by allowing data to be combined across mice and sessions.

Optogenetic Manipulation

To disrupt cortical activity during behavior, we built a laser scanning system that can direct laser stimulation unilaterally or bilaterally across the whole dorsal cortex surface. A collimated beam of blue light (470 nm) from a laser (SSL-473-0100-10TN-D-LED, Sanctity Laser) was fed into a 2D galvo system (GVS 002, Thorlabs) that was directed onto cortical surface using custom written tool boxes. The system contained an additional path to simultaneously visualize the cortical surface using a camera (BFS-U3-16S2C-CS, TELEDYNE FLIR). Using this system, we directed blue light with a beam diameter of 400 µm (full width half maximum) bilaterally at 30 Hz. Laser power at the stimulation site on the cortical surface was set between 10-15 mW. We bilaterally inhibited cortical areas identified from regions active during the feeding behavior task: FLA (1.6 mm anterior, 2.3 mm lateral), FLP(0.5mm anterior, 3.5 mm lateral), Frontal (2 mm anterior, 1 mm lateral) and Parietal (-1.2 mm posterior, 1.2 mm lateral). Using median onset times associated with lick, pellet in mouth and handlift from previous behavior trials, we turned on the stimulation prior to median lick onset time or during licking prior to median pellet in mouth onset time or after pellet in mouth but prior to median handlift onset time or after hand lift onset time during manipulation, bilaterally inhibiting each of the four ROIs for durations ranging from 5 to 7 seconds. The inhibition was randomly turned on between control trials where we did not provide any laser stimulation.

Neural and behavior data analysis

All neural and behavior analysis was performed on MATLAB v2018b.

Wakeful resting state analysis

Mice were first habituated to head fixation in the setup as described earlier. We imaged and extracted calcium dynamics at 30 fps (as described earlier) across the dorsal cortex for 3 minutes from 6 mice for each PN across two sessions on different days. We also simultaneously video recorded behavior at 20 fps. We filtered the calcium activity between 0.01Hz and 5 Hz per pixel to remove the extremely low frequency fluctuations and high frequency noise using 100 order finite impulse response bandpass filter. Power spectral density plots from both PNs during wakeful resting state indicated activity frequency was well below 5 Hz (Extended data 1d). Since most of the calcium activity was well below 5 Hz we also band pass filtered behavior videos between 0.01 and 5 Hz to retain the low frequency components of movements. To obtain time varying behavior variance signal, we computed the differential for each pixel in a video frame across time to obtain motion energy [69] and then computed variance for each frame of the motion energy video (Fig. 1c black trace). We resampled these traces to match sampling rate of calcium activity (30 Hz) using resample function in MATLAB. Time points when behavior variance exceeded 0.2 times the standard deviation were classified as active periods and remaining as quiescent. We then split calcium activity videos into active and quiescent episodes aligned with these time stamps and extracted variance per pixel across time for each episode to obtain variance maps. We then peak normalized these maps and averaged them across mice and sessions (Fig. 1d). To compute neural variance explained by spontaneous behavior, we performed singular value decomposition (SVD) of both calcium activity ($C_{n,t,}$ n: number of pixels, t: number of time points) and motion energy videos ($dB_{b,t} / dt$, b: number of pixels, t:

number of time points) and extracted the top 200 temporal components ($S*V^T$) from each decomposition (Extended data 3b). We then extracted amplitudes of the motion energy temporal components by computing the absolute value of their Hilbert transforms (Extended data 3b). We then built a liner encoding model using these 200 amplitude signals as independent variables to explain the top 200 temporal components of the calcium activity (Extended data 3b). We performed 5 fold cross validation of the model to obtain the cross validated R^2 [69].

$$SVD[\frac{dB_{b,t}}{dt}] = U^B_{b,t} * S^B_{t,t} * V^{B'}_{t,t}\ , \text{t} < \text{b}$$

$$Abs[\ Hilbert\ [\ [S^B_{200,200} * V^{B'}_{200,t}]'\ ]\ ] = X_{t,k}, \text{k} = 200$$

$$SVD\ [\ C_{n,t}\ ]\ = U^C_{n,t} * S^C_{t,t} * V^{C'}_{t,t}\ , \text{t} < \text{n}$$

$$[S^C_{200,200}\ *\ V^{C'}_{200,t}\ ]' = Y_{t,d}, \text{d} = 200$$

$$Y_{i,d} = \beta_{d,0} + \sum_{k=1}^{200} \beta_{d,k} X_{i,k} + \varepsilon_i, \forall\ 1 \le \text{d} \le 200, 1 \le \text{i} \le \text{t}$$

To compute variance explained by each body part, we first defined a window around each body part (Fig. 1f inset) and extracted motion energy within those windows as described earlier ($dB^{bp}_{b,t}/\ dt$, b: number of pixels, t: number of time points, bp: body part). We then extracted amplitudes (absolute of their Hilbert transforms) from each pixel of the motion energy video and averaged them within each window to obtain a time varying amplitude signal associated with movement of each body part ($x^{bp}_{t,1}$, Extended data 3c). We built a linear model using z-scored amplitude signal per body part as independent variables to explain the top 200 SVD temporal components of calcium activity ($Y_{t,d}$, t: number of time points, d: number of dimensions). We performed 5 fold cross validation to obtain the cross validated R^2 associated with each body part. For both linear encoding models we used ridge regression and identified the optimal lambda for each session from a range of values using 5 fold cross validation. To obtain the spatial map of transformed regression weights ($M^{bp}_{n,1}$, n: number of pixels, bp: body part), we computed the dot product between the model regression weights associated with each body part and the corresponding top 200 SVD spatial components (U) and transformed the resulting vector to a 2D matrix with dimensions matching the calcium activity frame.

$$\text{Avg}\ [\ \text{Abs}\ [\ \text{Hilbert}\ [\ \frac{\text{dB}^{\text{bp}}_{\text{b,t}}}{\text{dt}}\ ]\ ]\ ]' = x^{bp}_{t,1}\ , \forall\ \text{bp} \in \{\text{forelimb, mouth, nose, whiskers}\}$$

$$SVD\ [\ C_{n,t}\ ] = U_{n,t} * S_{t,t} *\ V'_{t,t}\ , \text{t}<\text{n}$$

$$[S_{200,200} * V'_{200,t}]' = Y_{t,d}, \text{d} = 200$$

$$Y_{i,d} = \beta^0_d + \beta^{forelimb}_d X^{forelimb}_i + \beta^{mouth}_d X^{mouth}_i + \beta^{nose}_d X^{nose}_i + \beta^{whiskers}_d X^{whiskers}_i + \varepsilon_i,$$
$$\forall\ 1 \le \text{d} \le 200, 1 \le \text{i} \le \text{t}$$

$$M^{bp}_{n,1} = U_{n,200} * \beta^{bp}_{200,1}\ , \forall\ bp \in \{forelimb, mouth, nose, whiskers\}$$

Sensory stimulation analysis

Before stimulation, mice were injected with chlorprothixene (1 mg/Kg i.p.) and maintained under light isoflurane anesthesia (0.8-1% with O_2). We then placed a custom designed cardboard attached to two piezo actuators (BA5010, PeizoDrive) close to left whisker pad between whiskers and just below the upper and lower lip. We also placed an orange LED close to dorsal region of the left eye. We used an Arduino Uno Rev3 (A00006, Arduino) to drive the piezo and LED. A single trial consisted of 3 seconds baseline followed by whisker stimulation at 25 Hz for 1 second, 3 second delay, orofacial stimulation at 25 Hz for 1 second, 3 second delay, blinking visual stimulus at about 16 Hz for 1 second followed by an additional 3 seconds before starting the next trial. We recorded one session per day consisting of 20 trials. To extract temporal traces, we used spatial maps obtained by averaging IT^{PlxnD1} activity per pixel during the 1 second stimulation period in response to each sensory stimulation. We identified centers of peak activity in each map and used a circular window of 560 µm diameter to extract signals within the circular mask and average them per frame.

Feeding behavior analysis

To identify sequential activation pattern during feeding behavior, we extracted frames one second before and one second after pellet in mouth onset for all trials across mice and sessions. Since each frame is registered to the allen CCFv3, we computed mean for each pixel at every sampling point to obtain an average activation map at each time point centered around pellet in mouth.

To identify activation maps associated with specific behavior event, we used a linear modelling approach. We generated binary time stamps associated with each behavior event as independent variables. For a single trial the lick variable consisted of ‘ones’ 0.3 seconds before lick onset to the start of pellet in mouth onset and ‘zeros’ at all other time points. The pellet in mouth variable consisted of ‘ones’ from start of pim onset to hand lift onset and ‘zeros’ everywhere else. The hand lift variable consisted of ‘ones’ from start of hand lift onset to 0.5 seconds after and ‘zeroes’ everywhere else. The handling and chew variables similarly contained ‘ones’ at time stamps classified by the handling and chew classifier previously described and zeros everywhere else. We then concatenated these variables vertically across trials within a session to generate the independent variable matrix ($X_{t,5,}$ t: number of time points). We then combined calcium activity across trials within a session ($C_{n,t}$, n: number of pixels, t: number of time points *)* and performed SVD to obtain top 200 temporal components ($S*V^T$) and used a linear model to fit the independent behavior variables to the SVD temporal components obtained from neural activity. We then computed a dot product between the regression weights obtain from the model for each behavior variable and spatial components (U) of the neural activity SVD to transform the regression weights into a spatial map (M) of regions associated with each behavior event.

$$SVD\,[\,C_{n,t}\,] = U_{n,t} * S_{t,t} * V'_{t,t}\ ,\ t<n$$

$$[S_{200,200} * V'_{200,t}]' = Y_{t,200}$$

$$Y_{i,d} = \beta_d^0 + \beta_d^{lick} X_i^{lick} + \beta_d^{pim} X_i^{pim} + \beta_d^{handlift} X_i^{handlift} + \beta_d^{handle} X_i^{handle} + \beta_d^{chew} X_i^{chew} + \varepsilon_i,$$
$$\forall\ 1 \le d \le 200,\ 1 \le i \le t$$

$$M_{n,1}^{event} = U_{n,200} * \beta_{200,1}^{event}\ ,\ \forall\ event \in \{lick,\ pim,\ handlift,\ handle,\ chew\}$$

To determine the significance of each independent variable in the model, we first measured the variance explained (R2) from the full model. We then measured the variance explained from a reduced model with time stamps for only one of the variable randomly shuffled and computed the difference in explained variance between the full and reduced model for each variable (delta R2). We computed the distribution of delta R2 for each variable by randomly shuffling time stamps 1000 times per session and measured the difference between full and reduced model and estimated its significance by quantifying the proportion of delta R2 greater than 0 (Extended data 5d). All variables for both PNs significantly contributed to the model with $p<0.005$ (Extended data 5d).
To identify the center of activation so as to extract temporal traces, we first calculated the average activity per pixel for 1 second before to 2 seconds after pim onset across mice and sessions (Fig. 3a,d). We then applied a mask containing mouth and nose primary sensory dorsal cortex region (as labeled by the Allen ccf V3) over the IT^{PlxnD1} activation map and identified center of peak activation and used it as the center of Frontolateral Posterior node (Fig. 3d, orange). Similarly we used MOs and MOp mask over IT^{PlxnD1} activation map to identify the center of Frontolateral Anterior node (Fig 3d, magenta). We used MOs mask over the PT^{Fezf2} activation map to identify the center of frontal node (Fig 3a, dark brown) and a few cortical regions in the posterior area (RSP_{agl}, VIS_{am}, VIS_{a}, $SS_{p\text{-}tr}$, $SS_{p\text{-}ll}$, $SS_{p\text{-}ul}$, $SS_{p\text{-}un}$, VIS_{rl}, $SS_{p\text{-}bfd}$) to identify the center of parietal node (Fig 3a, light brown). We used a circular window mask of 560 µm diameter around these centers to extract signals within these masks and averaged them per frame to obtain temporal dynamics from each node.

To extract peak rate of change, we first smoothened raw calcium activity signals centered to either lick onset for PT^{Fezf2} activity in the parietal and frontal node or centered to PIM onset for IT^{PlxnD1} activity in FLA and FLP using a 3rd order Savitzky-Golay (sgolayfilt) filter in MATLAB with a frame length parameter of 7. We then computed its first differential (Extended data 6a) and extracted the peak value between 1 second before to start of lick onset for PT^{Fezf2} activity in parietofrontal nodes and from 0.1 second before to 0.1 second after PIM onset for IT^{PlxnD1} activity in the frontolateral nodes.
To identify distinct activation clusters using Linear Discriminant Analysis (LDA), we first combined temporal activity centered to PIM onset from all trials within an ROI from both PNs along the temporal dimension. We then concatenated the PN type class labels associated with each trial and performed LDA on the activity matrix and class labels using the LDA toolbox (Dwinnell, 2021). (LDA: Linear Discriminant Analysis (https://www.mathworks.com/matlabcentral/fileexchange/29673-lda-linear-discriminant-analysis), MATLAB Central File Exchange. Retrieved December 28, 2021.). We then projected the temporal activity matrix on the first two dimensions identified by the analysis and colored them based on PN type to visualize clusters.

Ketamine anesthetized state analysis

To measure cortical dynamics under anesthesia we injected a mixture of Ketamine (87.5 $mgKg^{-1}$) / Xylazine (12.5 $mgKg^{-1}$) i.p. in each mouse and measure activity for 3 minutes at 30 Hz as described earlier. We used a 560 µm diameter circular mask and extracted average activity per frame within the mask across time to obtain signals from specific regions. We used Chornux [70] toolbox to calculate multi-taper spectrograms and relative power spectral densities. To obtain space time plot (Fig. 7f), we extracted pixels across a one dimensional slice of cortical surface and visualized calcium dynamics for each pixel in the slice across time.

To visualize the most dominant spatial activation pattern, we used seqNMF as described previously [39,40]. Briefly, the calcium activity was first band pass filtered between 0.01 Hz and 5 Hz. Since seqNMF is applied to non-negative matrices, values below zero were set to 0. This 3D matrix is transformed to a 2D matrix of pixels x time and seqNMF with parameters; sequence length: 30 (1 second), number of dimensions: 10 and lambda: 0.01 was used to obtain the most dominant sequence. Across a range of lambda values seqNMF identified just one sequence for both IT^{PlxnD1} and PT^{Fezf2} accounting for greater than 80% of variance. To identify most dominant sequence across mice and sessions, the first 20 seconds of activity from each mouse and session with a PN type was concatenated along the temporal dimension. We then used seqNMF to identify the most dominant sequence for each PN type as described above (Extended data 9d).

References

1 Bota, M., Sporns, O. & Swanson, L. W. Architecture of the cerebral cortical association connectome underlying cognition. *Proc Natl Acad Sci U S A* **112**, E2093-2101, doi:10.1073/pnas.1504394112 (2015).

2 Van Essen, D. C. & Glasser, M. F. Parcellating Cerebral Cortex: How Invasive Animal Studies Inform Noninvasive Mapmaking in Humans. *Neuron* **99**, 640-663, doi:10.1016/j.neuron.2018.07.002 (2018).

3 Hubel, D. H. & Wiesel, T. N. Shape and arrangement of columns in cat's striate cortex. *J Physiol* **165**, 559-568, doi:10.1113/jphysiol.1963.sp007079 (1963).

4 Mountcastle, V. B., Davies, P. W. & Berman, A. L. Response properties of neurons of cat's somatic sensory cortex to peripheral stimuli. *J Neurophysiol* **20**, 374-407, doi:10.1152/jn.1957.20.4.374 (1957).

5 Hubel David, H. & Wiesel Torsten, N. (New York, NY: Oxford University Press, 2005).

6 Douglas, R. J. & Martin, K. A. Mapping the matrix: the ways of neocortex. *Neuron* **56**, 226-238, doi:S0896-6273(07)00778-7 [pii] 10.1016/j.neuron.2007.10.017 (2007).
7 Harris, K. D. & Shepherd, G. M. The neocortical circuit: themes and variations. *Nat Neurosci* **18**, 170-181, doi:10.1038/nn.3917 (2015).
8 Markram, H. *et al.* Reconstruction and Simulation of Neocortical Microcircuitry. *Cell* **163**, 456-492, doi:10.1016/j.cell.2015.09.029 (2015).
9 Lerner, T. N., Ye, L. & Deisseroth, K. Communication in Neural Circuits: Tools, Opportunities, and Challenges. *Cell* **164**, 1136-1150, doi:10.1016/j.cell.2016.02.027 (2016).
10 Engel, T. A., Scholvinck, M. L. & Lewis, C. M. The diversity and specificity of functional connectivity across spatial and temporal scales. *Neuroimage* **245**, 118692, doi:10.1016/j.neuroimage.2021.118692 (2021).
11 Huang, Z. J. Toward a genetic dissection of cortical circuits in the mouse. *Neuron* **83**, 1284-1302, doi:10.1016/j.neuron.2014.08.041 (2014).
12 Tasic, B. *et al.* Shared and distinct transcriptomic cell types across neocortical areas. *Nature* **563**, 72-78, doi:10.1038/s41586-018-0654-5 (2018).
13 Gamanut, R. *et al.* The Mouse Cortical Connectome, Characterized by an Ultra-Dense Cortical Graph, Maintains Specificity by Distinct Connectivity Profiles. *Neuron* **97**, 698-715 e610, doi:10.1016/j.neuron.2017.12.037 (2018).
14 Zingg, B. *et al.* Neural networks of the mouse neocortex. *Cell* **156**, 1096-1111, doi:10.1016/j.cell.2014.02.023 (2014).
15 Oh, S. W. *et al.* A mesoscale connectome of the mouse brain. *Nature* **508**, 207-214, doi:10.1038/nature13186 (2014).
16 Harris, J. A. *et al.* Hierarchical organization of cortical and thalamic connectivity. *Nature* **575**, 195-202, doi:10.1038/s41586-019-1716-z (2019).
17 Munoz-Castaneda, R. *et al.* Cellular anatomy of the mouse primary motor cortex. *Nature* **598**, 159-166, doi:10.1038/s41586-021-03970-w (2021).
18 Gozzi, A. & Schwarz, A. J. Large-scale functional connectivity networks in the rodent brain. *Neuroimage* **127**, 496-509, doi:10.1016/j.neuroimage.2015.12.017 (2016).
19 Smith, S. M. *et al.* Functional connectomics from resting-state fMRI. *Trends Cogn Sci* **17**, 666-682, doi:10.1016/j.tics.2013.09.016 (2013).
20 Steinmetz, N. A. *et al.* Neuropixels 2.0: A miniaturized high-density probe for stable, long-term brain recordings. *Science* **372**, doi:10.1126/science.abf4588 (2021).
21 Svoboda, K., Helmchen, F., Denk, W. & Tank, D. W. Spread of dendritic excitation in layer 2/3 pyramidal neurons in rat barrel cortex in vivo. *Nat Neurosci* **2**, 65-73, doi:10.1038/4569 (1999).
22 Cardin, J. A., Crair, M. C. & Higley, M. J. Mesoscopic Imaging: Shining a Wide Light on Large-Scale Neural Dynamics. *Neuron* **108**, 33-43, doi:10.1016/j.neuron.2020.09.031 (2020).
23 Allen, W. E. *et al.* Global Representations of Goal-Directed Behavior in Distinct Cell Types of Mouse Neocortex. *Neuron* **94**, 891-907 e896, doi:10.1016/j.neuron.2017.04.017 (2017).
24 Musall, S., Kaufman, M. T., Juavinett, A. L., Gluf, S. & Churchland, A. K. Single-trial neural dynamics are dominated by richly varied movements. *Nat Neurosci* **22**, 1677-1686, doi:10.1038/s41593-019-0502-4 (2019).
25 Wekselblatt, J. B., Flister, E. D., Piscopo, D. M. & Niell, C. M. Large-scale imaging of cortical dynamics during sensory perception and behavior. *J Neurophysiol* **115**, 2852-2866, doi:10.1152/jn.01056.2015 (2016).
26 Gilad, A., Gallero-Salas, Y., Groos, D. & Helmchen, F. Behavioral Strategy Determines Frontal or Posterior Location of Short-Term Memory in Neocortex. *Neuron* **99**, 814-828 e817, doi:10.1016/j.neuron.2018.07.029 (2018).
27 Kauvar, I. V. *et al.* Cortical Observation by Synchronous Multifocal Optical Sampling Reveals Widespread Population Encoding of Actions. *Neuron* **107**, 351-367 e319, doi:10.1016/j.neuron.2020.04.023 (2020).

28 Ma, Y. *et al.* Resting-state hemodynamics are spatiotemporally coupled to synchronized and symmetric neural activity in excitatory neurons. *Proc Natl Acad Sci U S A* **113**, E8463-E8471, doi:10.1073/pnas.1525369113 (2016).
29 Vesuna, S. *et al.* Deep posteromedial cortical rhythm in dissociation. *Nature* **586**, 87-94, doi:10.1038/s41586-020-2731-9 (2020).
30 Xiao, D. *et al.* Mapping cortical mesoscopic networks of single spiking cortical or sub-cortical neurons. *Elife* **6**, doi:10.7554/eLife.19976 (2017).
31 Matho, K. S. *et al.* Genetic dissection of the glutamatergic neuron system in cerebral cortex. *Nature* **598**, 182-187, doi:10.1038/s41586-021-03955-9 (2021).
32 Shepherd, G. M. G. & Yamawaki, N. Untangling the cortico-thalamo-cortical loop: cellular pieces of a knotty circuit puzzle. *Nat Rev Neurosci* **22**, 389-406, doi:10.1038/s41583-021-00459-3 (2021).
33 Hooks, B. M. Sensorimotor Convergence in Circuitry of the Motor Cortex. *Neuroscientist* **23**, 251-263, doi:10.1177/1073858416645088 (2017).
34 Mathis, A. *et al.* DeepLabCut: markerless pose estimation of user-defined body parts with deep learning. *Nat Neurosci* **21**, 1281-1289, doi:10.1038/s41593-018-0209-y (2018).
35 Ragan, T. *et al.* Serial two-photon tomography for automated ex vivo mouse brain imaging. *Nat Methods* **9**, 255-258, doi:10.1038/nmeth.1854 (2012).
36 Tyson, A. L. *et al.* Tools for accurate post hoc determination of marker location within whole-brain microscopy images. *bioRxiv* (2021).
37 Niedworok, C. J. *et al.* aMAP is a validated pipeline for registration and segmentation of high-resolution mouse brain data. *Nat Commun* **7**, 11879, doi:10.1038/ncomms11879 (2016).
38 Whitesell, J. D. *et al.* Regional, Layer, and Cell-Type-Specific Connectivity of the Mouse Default Mode Network. *Neuron* **109**, 545-559 e548, doi:10.1016/j.neuron.2020.11.011 (2021).
39 MacDowell, C. J. & Buschman, T. J. Low-Dimensional Spatiotemporal Dynamics Underlie Cortex-wide Neural Activity. *Curr Biol* **30**, 2665-2680 e2668, doi:10.1016/j.cub.2020.04.090 (2020).
40 Mackevicius, E. L. *et al.* Unsupervised discovery of temporal sequences in high-dimensional datasets, with applications to neuroscience. *Elife* **8**, doi:10.7554/eLife.38471 (2019).
41 Shepherd, G. M. Corticostriatal connectivity and its role in disease. *Nat Rev Neurosci* **14**, 278-291, doi:10.1038/nrn3469 (2013).
42 Brodmann, K. *Vergleichende Lokalisationslehre der Grosshirnrinde in ihren Prinzipien dargestellt auf Grund des Zellenbaues*. (Barth, 1909).
43 Vogt, C. & Vogt, O. *Allgemeine ergebnisse unserer hirnforschung*. Vol. 21 (JA Barth, 1919).
44 von Economo, C. F. & Koskinas, G. N. *Die cytoarchitektonik der hirnrinde des erwachsenen menschen*. (J. Springer, 1925).
45 Adams, D. L. & Horton, J. C. Capricious expression of cortical columns in the primate brain. *Nat Neurosci* **6**, 113-114, doi:10.1038/nn1004 (2003).
46 da Costa, N. M. & Martin, K. A. Whose Cortical Column Would that Be? *Front Neuroanat* **4**, 16, doi:10.3389/fnana.2010.00016 (2010).
47 Rakic, P. Confusing cortical columns. *Proc Natl Acad Sci U S A* **105**, 12099-12100, doi:10.1073/pnas.0807271105 (2008).
48 Douglas, R. J. & Martin, K. A. A functional microcircuit for cat visual cortex. *J Physiol* **440**, 735-769, doi:10.1113/jphysiol.1991.sp018733 (1991).
49 Arlotta, P. *et al.* Neuronal subtype-specific genes that control corticospinal motor neuron development in vivo. *Neuron* **45**, 207-221, doi:10.1016/j.neuron.2004.12.036 (2005).
50 Greig, L. C., Woodworth, M. B., Galazo, M. J., Padmanabhan, H. & Macklis, J. D. Molecular logic of neocortical projection neuron specification, development and diversity. *Nat Rev Neurosci* **14**, 755-769, doi:10.1038/nrn3586 (2013).
51 Li, N., Chen, T. W., Guo, Z. V., Gerfen, C. R. & Svoboda, K. A motor cortex circuit for motor planning and movement. *Nature* **519**, 51-56, doi:10.1038/nature14178 (2015).

52 Takahashi, N. *et al.* Active dendritic currents gate descending cortical outputs in perception. *Nat Neurosci* **23**, 1277-1285, doi:10.1038/s41593-020-0677-8 (2020).
53 Tang, L. & Higley, M. J. Layer 5 Circuits in V1 Differentially Control Visuomotor Behavior. *Neuron* **105**, 346-354 e345, doi:10.1016/j.neuron.2019.10.014 (2020).
54 Waters, J. Sources of widefield fluorescence from the brain. *Elife* **9**, doi:10.7554/eLife.59841 (2020).
55 Huang, L. *et al.* Relationship between simultaneously recorded spiking activity and fluorescence signal in GCaMP6 transgenic mice. *Elife* **10**, doi:10.7554/eLife.51675 (2021).
56 Peters, A. J., Fabre, J. M. J., Steinmetz, N. A., Harris, K. D. & Carandini, M. Striatal activity topographically reflects cortical activity. *Nature* **591**, 420-425, doi:10.1038/s41586-020-03166-8 (2021).
57 Kvitsiani, D. *et al.* Distinct behavioural and network correlates of two interneuron types in prefrontal cortex. *Nature* **498**, 363-366, doi:10.1038/nature12176 (2013).
58 Whitlock, J. R. Posterior parietal cortex. *Curr Biol* **27**, R691-R695, doi:10.1016/j.cub.2017.06.007 (2017).
59 Lyamzin, D. & Benucci, A. The mouse posterior parietal cortex: Anatomy and functions. *Neurosci Res* **140**, 14-22, doi:10.1016/j.neures.2018.10.008 (2019).
60 Carandini, M. & Churchland, A. K. Probing perceptual decisions in rodents. *Nat Neurosci* **16**, 824-831, doi:10.1038/nn.3410 (2013).
61 Hovde, K., Gianatti, M., Witter, M. P. & Whitlock, J. R. Architecture and organization of mouse posterior parietal cortex relative to extrastriate areas. *Eur J Neurosci* **49**, 1313-1329, doi:10.1111/ejn.14280 (2019).
62 Olsen, G. M. *et al.* Organization of Posterior Parietal-Frontal Connections in the Rat. *Front Syst Neurosci* **13**, 38, doi:10.3389/fnsys.2019.00038 (2019).
63 Hwang, E. J. *et al.* Corticostriatal Flow of Action Selection Bias. *Neuron* **104**, 1126-1140 e1126, doi:10.1016/j.neuron.2019.09.028 (2019).
64 Andersen, R. A. & Cui, H. Intention, action planning, and decision making in parietal-frontal circuits. *Neuron* **63**, 568-583, doi:10.1016/j.neuron.2009.08.028 (2009).
65 Sherman, S. M. Thalamus plays a central role in ongoing cortical functioning. *Nat Neurosci* **19**, 533-541, doi:10.1038/nn.4269 (2016).
66 Yamawaki, N., Radulovic, J. & Shepherd, G. M. A Corticocortical Circuit Directly Links Retrosplenial Cortex to M2 in the Mouse. *J Neurosci* **36**, 9365-9374, doi:10.1523/JNEUROSCI.1099-16.2016 (2016).
67 Hooks, B. M. *et al.* Topographic precision in sensory and motor corticostriatal projections varies across cell type and cortical area. *Nat Commun* **9**, 3549, doi:10.1038/s41467-018-05780-7 (2018).
68 Wang, Q. *et al.* The Allen Mouse Brain Common Coordinate Framework: A 3D Reference Atlas. *Cell* **181**, 936-953 e920, doi:10.1016/j.cell.2020.04.007 (2020).
69 Stringer, C. *et al.* Spontaneous behaviors drive multidimensional, brainwide activity. *Science* **364**, 255, doi:10.1126/science.aav7893 (2019).
70 Bokil, H., Andrews, P., Kulkarni, J. E., Mehta, S. & Mitra, P. P. Chronux: a platform for analyzing neural signals. *J Neurosci Methods* **192**, 146-151, doi:10.1016/j.jneumeth.2010.06.020 (2010).

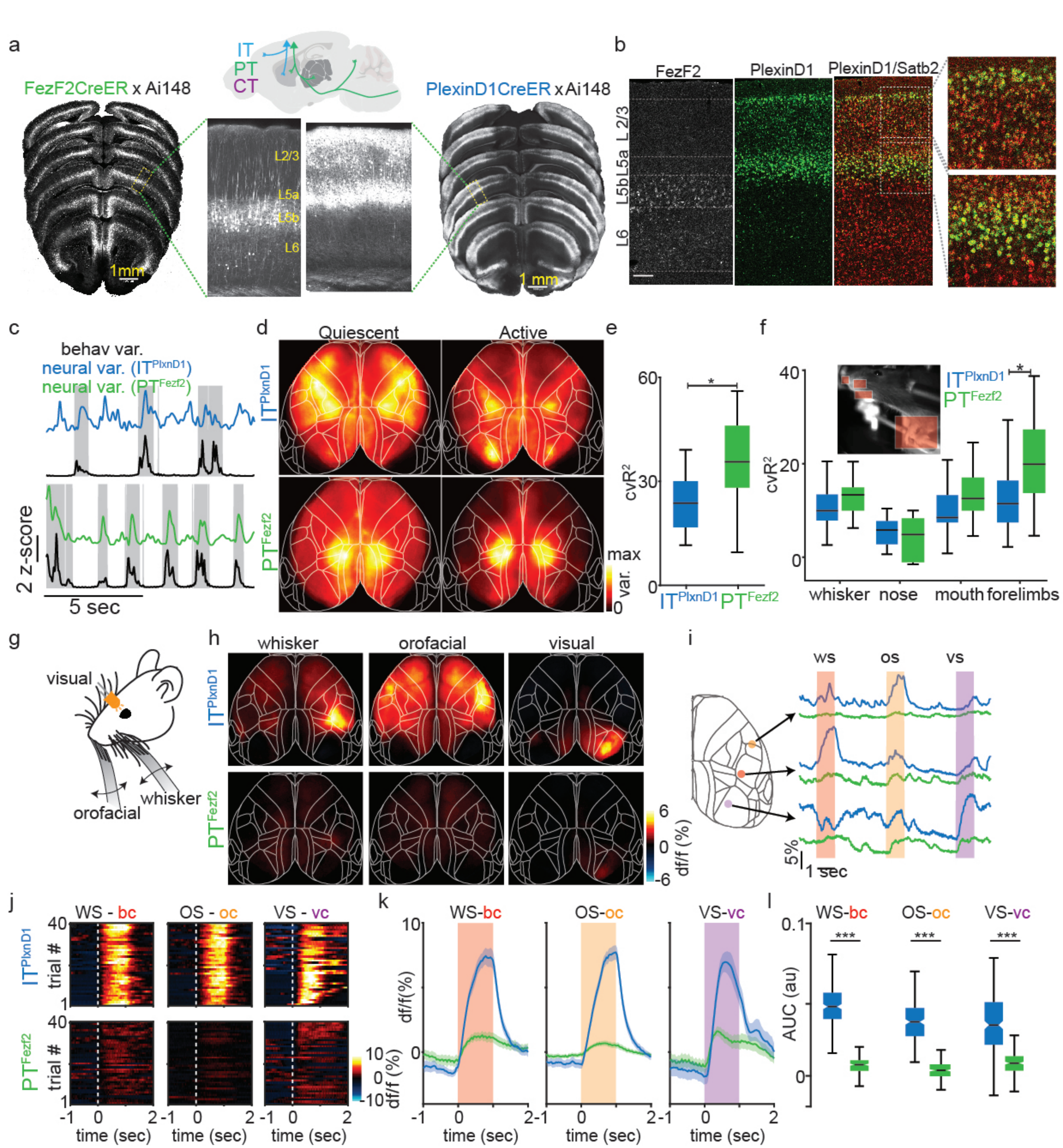
a
FezF2CreER x Ai148
IT
PT
CT
PlexinD1CreER x Ai148
L2/3
L5a
L5b
L6
1mm
1 mm
b
FezF2
PlexinD1
PlexinD1/Satb2
L2/3
L5a
L5b
L6
c
behav var.
neural var. (IT PlxnD1)
neural var. (PT Fezf2)
2 z-score
5 sec
d
Quiescent
Active
IT PlxnD1
PT Fezf2
max
var.
0
e
cvR²
60
30
0
IT PlxnD1
PT Fezf2
f
cvR²
40
20
0
IT PlxnD1
PT Fezf2
whisker
nose
mouth
forelimbs
g
visual
whisker
orofacial
h
whisker
orofacial
visual
IT PlxnD1
PT Fezf2
6
0
-6
df/f (%)
i
ws
os
vs
5%
1 sec
j
WS - bc
OS - oc
VS - vc
IT PlxnD1
PT Fezf2
trial #
40
1
time (sec)
10
0
-10
k
WS-bc
OS-oc
VS-vc
df/f(%)
10
0
-1
0
2
l
WS-bc
OS-oc
VS-vc
AUC (au)
0.1
0
***

figure 1

Figure 1. Distinct cortical activity patterns of IT^{PlxnD1} and PT^{Fezf2} during wakeful resting and upon sensory input

a. Serial two photon tomography images showing distribution of PT^{Fezf2} and IT^{PlxnD1} across dorsal cortex in *FezF2-CreER:Ai148* and *PlexinD1-CreER:Ai148* mice. Blue dashed lines indicate approximate transition from layer 1 to layer 2/3 to layer 5a to layer 5b to layer 6. Sagittal schematic depicts the major projection patterns of IT, PT, and CT neurons.
b. mRNA in situ images and distribution of *Fezf2*$^+$ (left), *PlexinD1*$^+$ (middle) cells. Double in situ overlaid (right) shows *Satb2*$^+$ in red and *PlexinD1*$^+$ in green. Note that *PlexinD1*$^+$ cells represent a subset of *Satb2*$^+$ IT cells.
c. Example z-scored variance trace of behavior from video recordings (black trace) and corresponding z-scored variance trace of neural activity from IT^{PlxnD1} (blue) and PT^{Fezf2} (green) from wide-field GCaMP6f imaging. Gray blocks indicate active episodes identified from behavior variance trace.
d. Average peak normalized variance maps of spontaneous neural activity during active and quiescent episodes (12 sessions from 6 mice each).
e. Distribution of the percentage of cross validated IT^{PlxnD1} and PT^{Fezf2} neural activity variance explained by full frame behavior variance obtained from a linear encoding model (12 sessions from 6 mice each, two-sided Wilcoxon rank sum test (*U=109, z=-2.34, p = 0.019)*).
f. Distribution of the percentage of cross validated IT^{PlxnD1} and PT^{Fezf2} neural activity variance explained by variance of specific body part movements obtained from the linear encoding model (12 sessions from 6 mice each, two-sided Wilcoxon rank sum test, whiskers (*U=171,z=1.18,p=0.24*), nose (*U=134, z=-0.89,p=0.47)*, mouth *(U=176, z=1.47, p=0.14)*, forelimbs *(U=188, z=2.16, p=0.03)*).
g. Illustration of unimodal sensory stimulation paradigm.
h. Mean activity maps of IT^{PlxnD1} and PT^{Fezf2} in response to corresponding unimodal sensory simulation (average of 12 sessions from 6 mice each).
i. Single trial IT^{PlxnD1} and PT^{Fezf2} activity within orofacial, whisker and visual areas during corresponding sensory stimulation.
j. Single trial heat maps of IT^{PlxnD1} and PT^{Fezf2} activity from whisker (bc), orofacial (oc) and visual cortex (vc) in response to corresponding sensory stimulus from 1 example mouse.
k. Mean temporal dynamics of IT^{PlxnD1} and PT^{Fezf2} activity in whisker (bc), orofacial (oc) and visual cortex (vc) in response to corresponding sensory stimulus (average of 240 trials in 12 sessions from 6 mice each, shaded region indicates ±2 s.e.m).
l. Distribution of IT^{PlxnD1} and PT^{Fezf2} activity intensity in whisker, orofacial and visual cortex in response to corresponding sensory stimulus (240 trials in 12 sessions from 6 mice each, two-sided Wilcoxon rank sum test, whisker stimulation *(U=85830, z=18.5, p=2e-76)*, orofacial stimulation *(U=85996, z=18.6,p=2e-77)*, visual stimulation *(U=82409, z=16.2, p=2e-59)*).

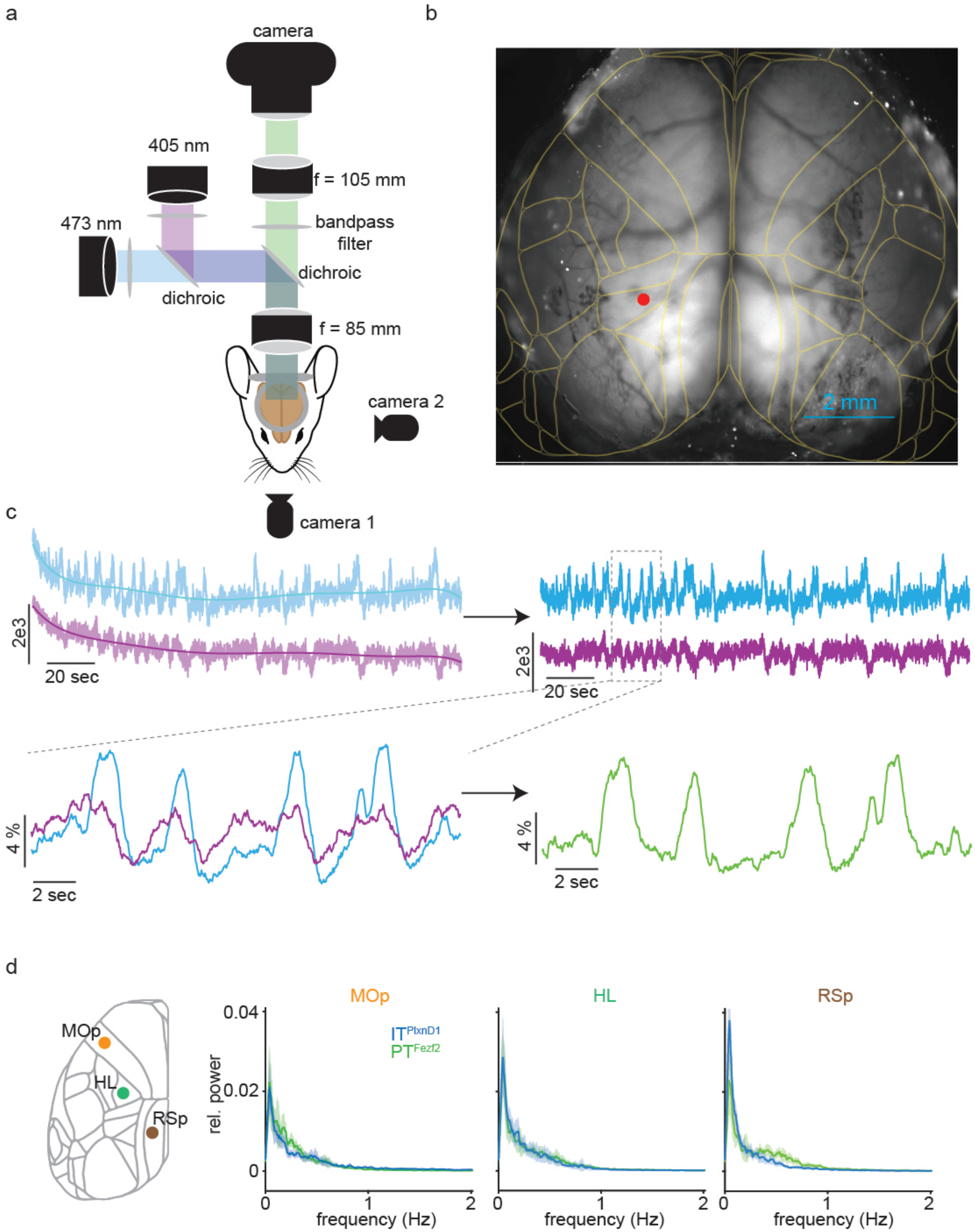

Extended data 1

Extended Data 1. Widefield imaging system layout and signal correction.

a. Schematic of the wide-field imaging system.
b. Example field of view of dorsal cortex obtained from the widefield imaging system overlaid with registered Allen map in yellow. Red dot indicates the location used to plot example traces in panel c.
c. Illustration of the method used to obtain final df/f signal for spontaneous recordings. Blue and violet traces indicate signal obtained during excitation with 473 nm and 405 nm respectively. Top left: raw signal. Top Right: signals after detrending. Bottom left: Zoomed in signals after normalizing to baseline (df/f). Bottom right: Final signal after regressing violet from blue trace.
d. Mean relative power spectral density of IT^{PlxnD1} (blue) and PT^{Fezf2} (green) activity from MOp, HL sensory and RSp during awake resting state condition (average of 12 sessions across 6 mice, shading around trace 2 s.e.m).

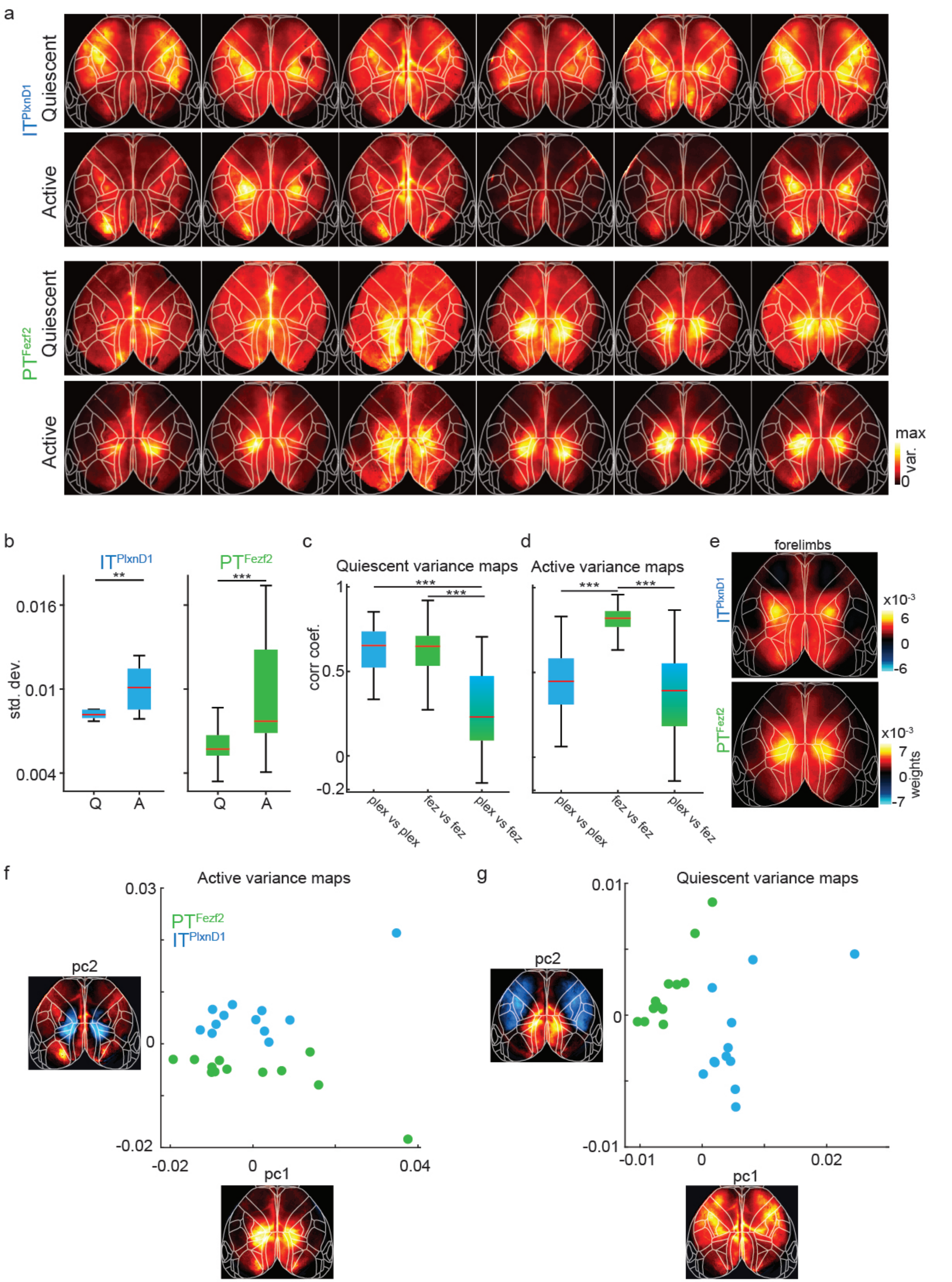

Extended data 2

Extended Data 2. IT^{PlxnD1} and PT^{Fezf2} activation patterns during wakeful resting state across mice.

a. Peak normalized variance maps for each mouse (in columns) during quiescent and active episodes averaged over two sessions each.
b. Distribution of standard deviations during quiescent (Q) versus active (A) episodes in IT^{PlxnD1} (blue) and PT^{Fezf2} (green) (12 sessions from 6 mice each, paired two-sided Wilcoxon signed rank test Quiescent vs. Active IT^{PlxnD1} *(U=77, p = 9.8e-4)*, PT^{Fezf2} *(U=78, p=4.8e-4)*).
c. Distribution of Pearson's correlation coefficients between quiescent variance maps within IT^{PlxnD1} (blue), PT^{Fezf2} (green) and between IT^{PlxnD1} & PT^{Fezf2} (blue green) (66 pairs within IT^{PlxnD1} & PT^{Fezf2} and 144 pairs between IT^{PlxnD1} & PT^{Fezf2} in 12 sessions from 6 mice each, Kruskal-Wallis test *($\chi^2(2) = 129.02$, $p = 9.6e\text{-}29$)* with Tukey-Kramer (alpha = 0.05) post hoc multiple comparison test $IT^{PlxnD1\ Vs.\ PlxnD1}$ Vs. $PT^{Fezf2\ Vs.\ Fezf2}$ *(p=0.86)* , $IT^{PlxnD1\ Vs.\ PlxnD1}$ Vs. IT/$PT^{PlxnD1\ Vs.\ Fezf2}$ *(p=5.9e-8)*, $PT^{Fezf2\ Vs.\ Fezf2}$ Vs. IT/$PT^{PlxnD1\ Vs.\ Fezf2}$ *(p=5.9e-8)*).
d. Distribution of Pearson's correlation coefficients between active variance maps within IT^{PlxnD1} (blue), PT^{Fezf2} (green) and between IT^{PlxnD1} and PT^{Fezf2} (blue green) (66 pairs within IT^{PlxnD1} & PT^{Fezf2} and 144 pairs between IT^{PlxnD1} & PT^{Fezf2} in 12 sessions from 6 mice each, Kruskal-Wallis test *($\chi^2(2) = 125.19$, $p = 6.5e\text{-}28$)* with Tukey-Kramer (alpha = 0.05) post hoc multiple comparison test $IT^{PlxnD1\ Vs.\ PlxnD1}$ Vs. $PT^{Fezf2\ Vs.\ Fezf2}$ *(p=5.9e-8)* , $IT^{PlxnD1\ Vs.\ PlxnD1}$ Vs. IT/$PT^{PlxnD1\ Vs.\ Fezf2}$ *(p=0.32)*, $PT^{Fezf2\ Vs.\ Fezf2}$ Vs. IT/$PT^{PlxnD1\ Vs.\ Fezf2}$ *(p=5.9e-8)*).
e. IT^{PlxnD1} (top) and PT^{Fezf2} (bottom) regression weight maps associated with forelimb movements obtained from the linear encoding model. PT^{Fezf2} was most active in parietal area while IT^{PlxnD1} was most active in hind limb sensory area
f. Distribution of IT^{PlxnD1} (blue) and PT^{Fezf2} (green) active variance maps projected to the subspace spanned by the top two principal components.
g. Distribution of IT^{PlxnD1} (blue) and PT^{Fezf2} (green) quiescent variance maps projected to the subspace spanned by the top two principal components.

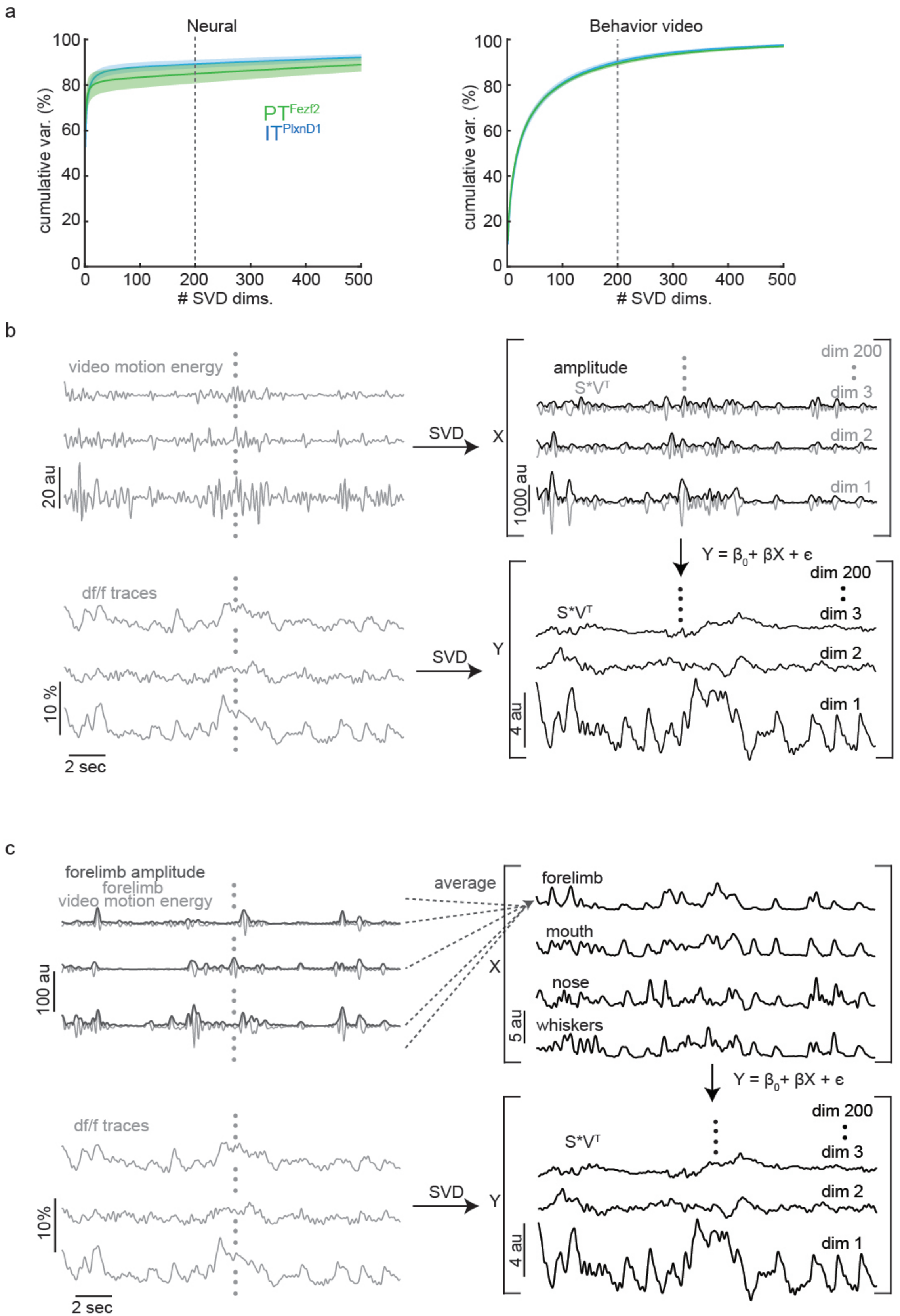

Extended data 3

Extended Data 3. Linear encoding model for measuring neural variance associated with behavior variance.

a. Left: Cumulative distribution of variance accounted by the corresponding singular value decomposition (SVD) temporal dimensions of IT^{PlxnD1} (blue) and PT^{Fezf2} (green) calcium activity. Right: Cumulative distribution of variance accounted by the corresponding SVD temporal dimensions of IT^{PlxnD1} (blue) and PT^{Fezf2} (green) behavior video motion energy (average of 12 sessions across 6 mice, shading around trace 2 s.e.m).
b. Illustration of the linear encoding model used to fit SVD temporal dimensions of behavior video to neural activity SVD temporal dimensions. Top left: traces indicate motion energy signal of example pixels from behavior video frames. Top right: Top three SVD temporal dimensions along with its amplitudes obtained by decomposing motion energy of behavior videos. Bottom left: calcium traces from exampled pixels corresponding to the behavior frame. Bottom right: Top three SVD temporal dimensions obtained by decomposing neural activity.
c. Illustration of the linear encoding model used to fit behavior variance within specific windows of the behavior video to the top 200 neural activity SVD temporal dimensions. Top left: traces indicate motion energy signal with its amplitude from example pixels within the forelimb window. Top right: Average of amplitudes from all pixels within the forelimb widow. Bottom left: calcium traces from exampled pixels corresponding to the behavior frame. Bottom right: Top three SVD temporal dimensions obtained by decomposing neural activity.

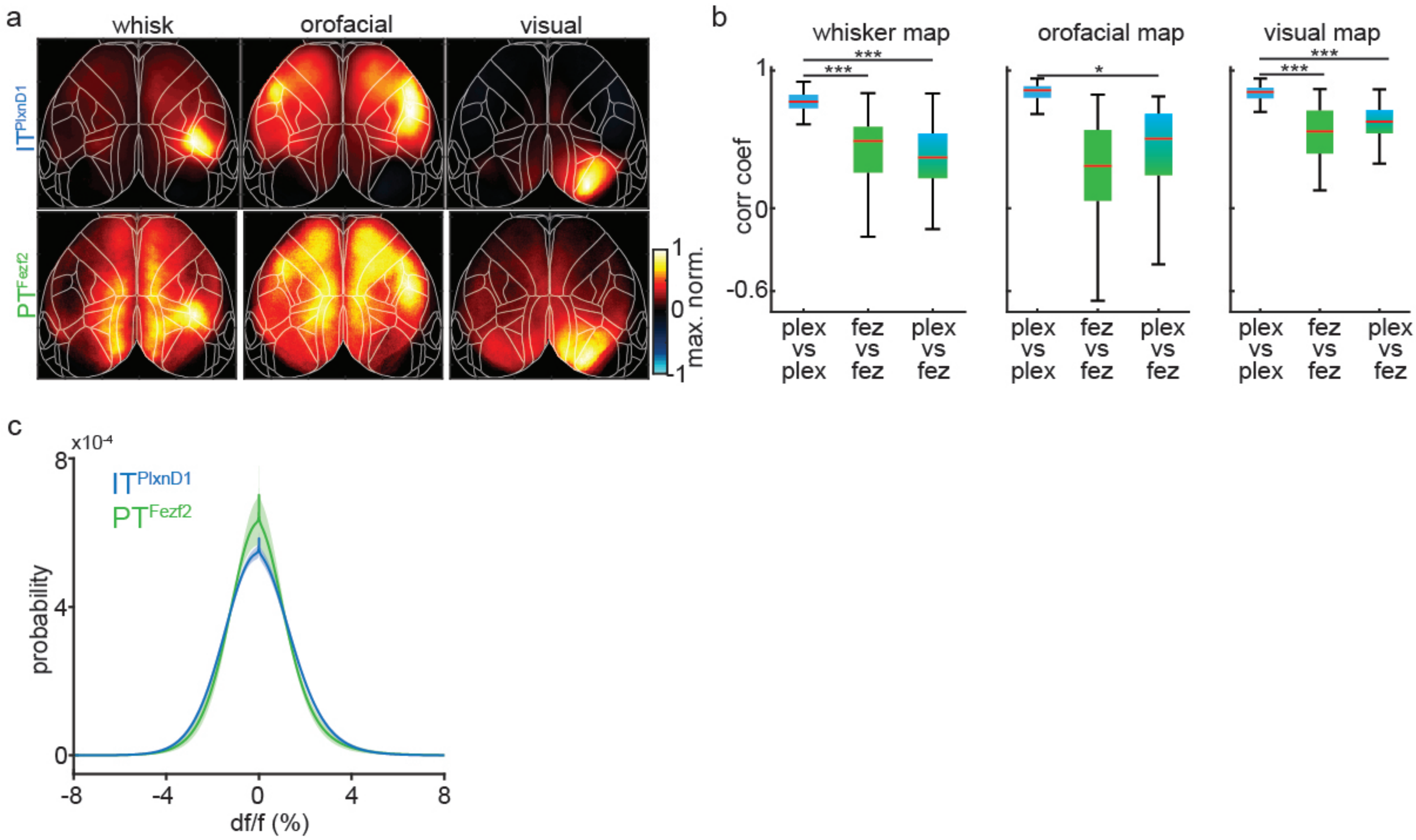

Extended data 4

Extended Data 4. Correlation of sensory response in IT^{PlxnD1} and PT^{Fezf2} across mice.

a. Mean peak normalized activity maps of IT^{PlxnD1} (top) and PT^{Fezf2} (bottom) in response to corresponding unimodal sensory simulation (average of 12 sessions from 6 mice each).
b. Distribution of Pearson's correlation coefficients between sensory activation maps within IT^{PlxnD1} (blue), PT^{Fezf2} (green) and between IT^{PlxnD1} and PT^{Fezf2} (blue green) (66 pairs within IT^{PlxnD1} & PT^{Fezf2} and 144 pairs between IT^{PlxnD1} & PT^{Fezf2} in 12 sessions from 6 mice each for all stimulations, whisker stimulation Kruskal-Wallis test *($\chi^2(2) = 120.32$, $p = 7.4e\text{-}27$)* with Tukey-Kramer (alpha = 0.05) post hoc multiple comparison test $IT^{PlxnD1\ Vs.\ PlxnD1}$ Vs. $PT^{Fezf2\ Vs.\ Fezf2}$ *(p=9.5e-10)* , $IT^{PlxnD1\ Vs.\ PlxnD1}$ Vs. $IT/PT^{PlxnD1\ Vs.\ Fezf2}$ *(p=9.5e-10)*, $PT^{Fezf2\ Vs.\ Fezf2}$ Vs. $IT/PT^{PlxnD1\ Vs.\ Fezf2}$ *(p=0.46)*, orofacial stimulation Kruskal-Wallis test *($\chi^2(2) = 141.64$, $p = 1.7e\text{-}31$)* with Tukey-Kramer (alpha = 0.05) post hoc multiple comparison test $IT^{PlxnD1\ Vs.\ PlxnD1}$ Vs. $PT^{Fezf2\ Vs.\ Fezf2}$ *(p=9.5e-10)* , $IT^{PlxnD1\ Vs.\ PlxnD1}$ Vs. $IT/PT^{PlxnD1\ Vs.\ Fezf2}$ *(p=9.5e-10)*, $PT^{Fezf2\ Vs.\ Fezf2}$ Vs. $IT/PT^{PlxnD1\ Vs.\ Fezf2}$ *(p=0.03)*, visual stimulation Kruskal-Wallis test *($\chi^2(2) = 130.05$, $p = 5.7e\text{-}29$)* with Tukey-Kramer (alpha = 0.05) post hoc multiple comparison test $IT^{PlxnD1\ Vs.\ PlxnD1}$ Vs. $PT^{Fezf2\ Vs.\ Fezf2}$ *(p=9.5e-10)* , $IT^{PlxnD1\ Vs.\ PlxnD1}$ Vs. $IT/PT^{PlxnD1\ Vs.\ Fezf2}$ *(p=9.5e-10)*, $PT^{Fezf2\ Vs.\ Fezf2}$ Vs. $IT/PT^{PlxnD1\ Vs.\ Fezf2}$ *(p=0.21)*).
c. Probability distribution of df/f values from IT^{PlxnD1} (blue) and PT^{Fezf2} (green) during wakeful resting state (average of 12 sessions from 6 mice each, shading around trace indicate ± 2 s.e.m).

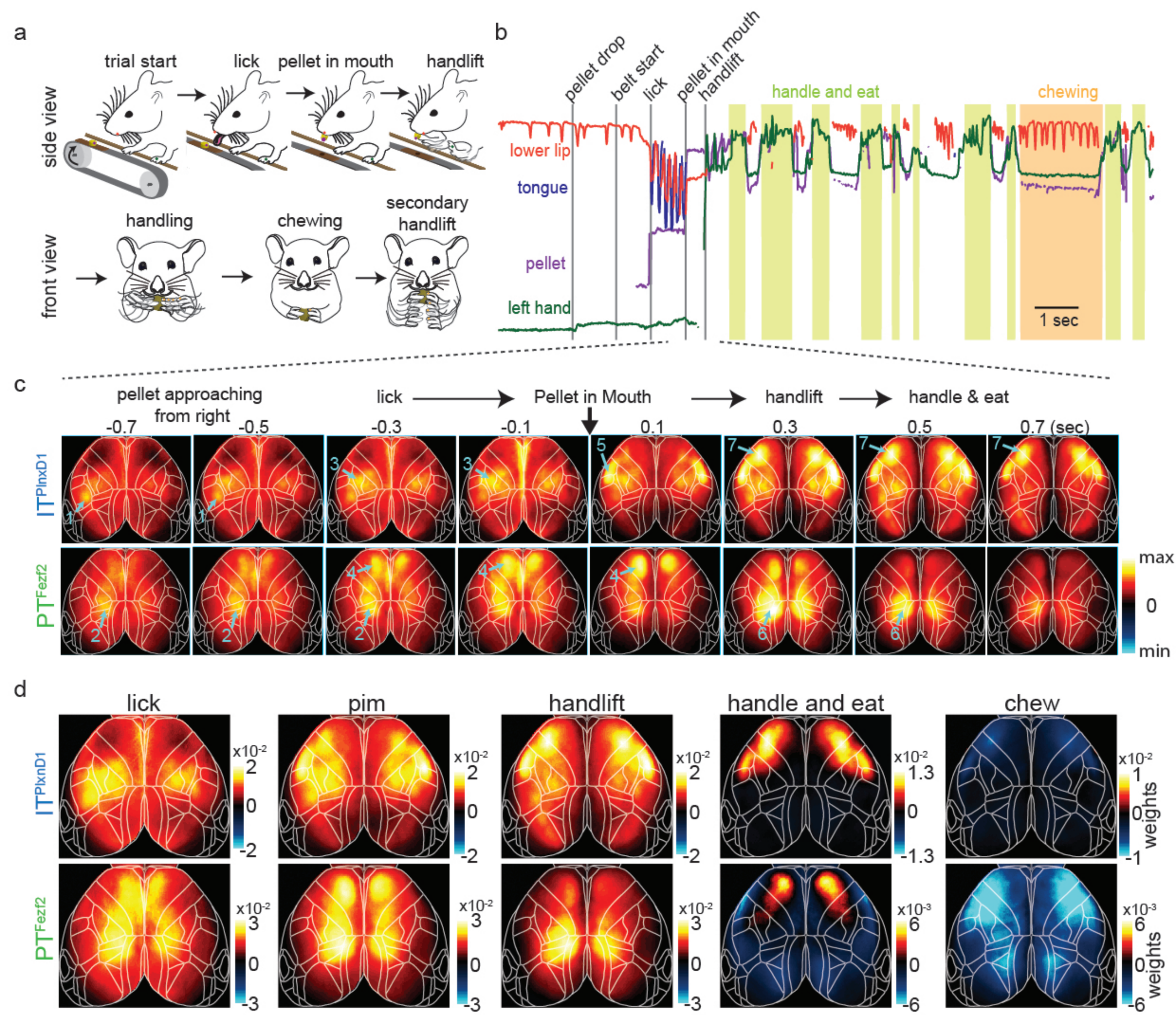
a
trial start
lick
pellet in mouth
handlift
side view
handling
chewing
secondary handlift
front view
b
pellet drop
belt start
lick
pellet in mouth
handlift
handle and eat
chewing
lower lip
tongue
pellet
left hand
1 sec
c
pellet approaching from right
lick
Pellet in Mouth
handlift
handle & eat
-0.7
-0.5
-0.3
-0.1
0.1
0.3
0.5
0.7 (sec)
ITPlxnD1
PTFezf2
max
0
min
d
lick
pim
handlift
handle and eat
chew
ITPlxnD1
PTFezf2
weights

figure 2

Figure 2. Distinct PT^{Fezf2} and IT^{PlxnD1} subnetworks tuned to different sensorimotor components of a feeding behavior

a. Schematic of the head-fixed feeding behavior showing the sequential sensorimotor components.
b. Example traces of tracked body parts and episodes of classified behavior events. Colored lines represent different body parts as indicated. light green shade: handle-and-eat episodes; orange shade: chewing episode).
c. Mean IT^{PlxnD1} and PT^{Fezf2} sequential activity maps during the feeding sequence before and after pellet-in-mouth (PIM) onset (IT^{PlxnD1} - 23 sessions from 6 mice, PT^{Fezf2} - 24 sessions from 5 mice). Note the largely sequential activation of areas and cell types indicated by arrows and numbers: 1) left barrel cortex (IT^{PlxnD1}) when right whiskers sensed approaching pellet; 2) parietal node (PT^{Fezf2}) while making postural adjustments as pellet arrives; 3) forelimb sensory area (IT^{PlxnD1}) with limb movements that adjusted grips of support bar as pellet approaches closer; 4) frontal node (PT^{Fezf2}) during lick; 5) orofacial sensory areas (FLP (Frontolateral Posterior), IT^{PlxnD1}) when pellet-in-mouth; 6) parietal node again during hand lift; 7) FLA (Frontolateral Anterior)-FLP (IT^{PlxnD1}) on handling and eating the pellet.
d. Spatial maps of IT^{PlxnD1} (top) and PT^{Fezf2} (bottom) regression weights from an encoding model associated with lick, PIM, hand lift, eating and handling, and chewing (IT^{PlxnD1} - 23 sessions from 6 mice, PT^{Fezf2} - 24 sessions from 5 mice).

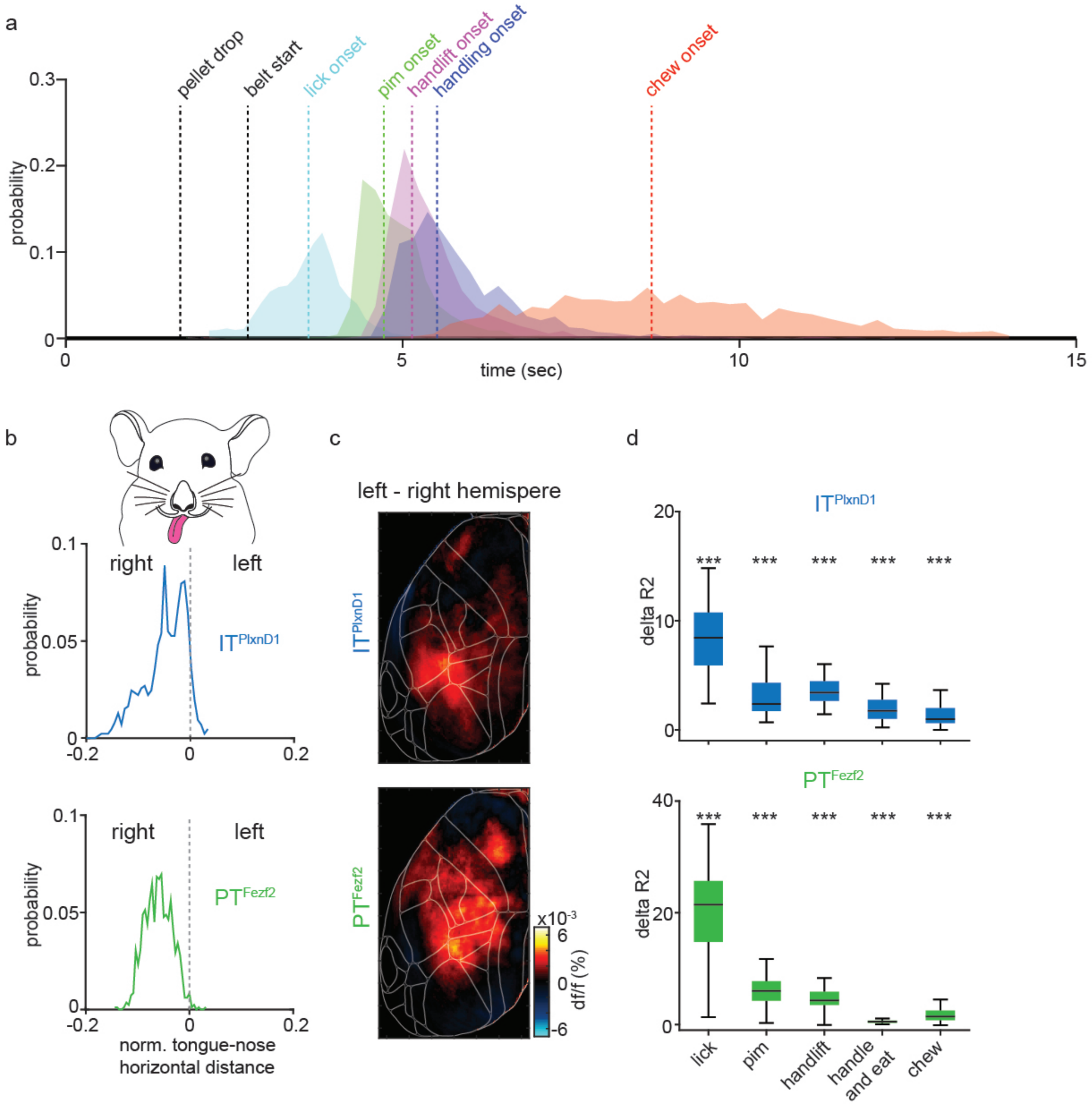

Extended data 5

Extended Data 5. Differential activation between cortical hemispheres during feeding sequence.

a. Probability distribution of onset of lick, PIM, hand lift, first handling event and first chew event across all mice and sessions.
b. Probability distribution of horizontal distance of tongue tip normalized to location of nose (top: IT^{PlxnD1} - 23 sessions from 6 mice, bottom: PT^{Fezf2} - 24 sessions from 5 mice).
c. Mean spatial maps of the difference between right and left hemisphere activity from IT^{PlxnD1} (top, 23 sessions from 6 mice) and PT^{Fezf2} (bottom, 24 sessions from 5 mice).
d. Distribution of the difference in variance explained between full and reduced model (delta R2, used in figure 2d) for each variable from IT^{PlxnD1} (top, 23 sessions from 6 mice) and PT^{Fezf2} (bottom, 24 sessions from 5 mice) ***$p<0.0005$.

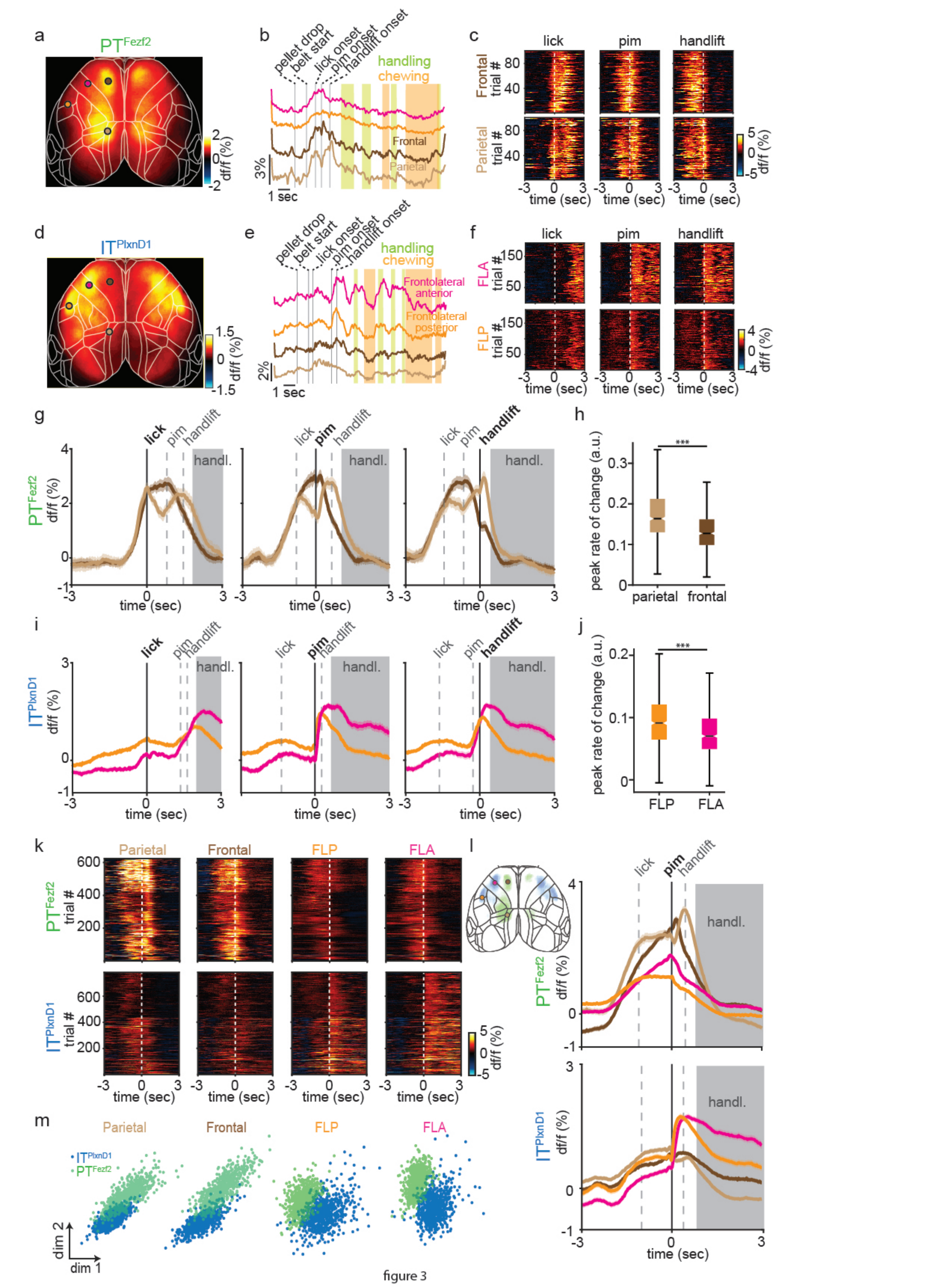
a
PTFezf2
df/f (%)
b
pellet drop
belt start
lick onset
pim onset
handlift onset
handling
chewing
Frontal
Parietal
3%
1 sec
c
lick
pim
handlift
Frontal
Parietal
trial #
time (sec)
df/f (%)
d
ITPlxnD1
e
Frontolateral anterior
Frontolateral posterior
2%
f
FLA
FLP
g
lick
pim
handlift
handl.
PTFezf2
h
peak rate of change (a.u.)
parietal
frontal
i
ITPlxnD1
j
FLP
FLA
k
Parietal
Frontal
FLP
FLA
l
m
dim 1
dim 2

figure 3

Figure 3. IT^{PlxnD1} and PT^{Fezf2} within frontolateral and parietofrontal nodes show distinct temporal dynamics during feeding behavior

a. Mean overall activity map of PT^{Fezf2} across the dorsal cortex during the feeding sequence from 1 second before to 2 seconds after PIM onset (24 sessions from 5 mice).
b. Example single PT^{Fezf2} activity traces from FLA (magenta), FLP (orange), frontal (dark brown) and parietal (light brown) nodes during feeding behavior; vertical bars indicate different behavior events.
c. Single trial heat maps of PT^{Fezf2} activities from frontal and parietal nodes centered to onset of licking, PIM, and hand lift (5 sessions from one example mouse).
d. Mean overall activity map of IT^{PlxnD1} across the dorsal cortex during the feeding sequence from 1 second before to 2 seconds after PIM onset (23 sessions from 6 mice).
e. Example single IT^{PlxnD1} activity traces from FLA, FLP, frontal and parietal nodes during feeding behavior.
f. Single trial heat maps of IT^{PlxnD1} activities from FLA and FLP nodes centered to onset of licking, PIM and hand lift (5 sessions from one example mouse).
g. Mean PT^{Fezf2} activity within frontal and parietal node centered to onset of lick, PIM, and hand lift. Grey dashed lines indicate median onset times of other events relative to centered event (5 sessions from one example mouse, shading around trace ±2 s.e.m). Grey shade indicates eating-handling episode.
h. Distribution of peak rate of change of PT^{Fezf2} activities from parietal and frontal node centered to lick onset (648 trials in 24 sessions from 5 mice each, two-sided Wilcoxon rank sum test *(U=334550, z=-12.7, p=4.7e-37)*).
i. Mean IT^{PlxnD1} activity within FLA and FLP centered to onset of lick, PIM, and hand lift; grey dashed lines indicate median onset times of other events relative to centered event (5 sessions from one example mouse, shading around trace ±2 s.e.m). Grey shade indicates eating-handling episode.
j. Distribution of peak rate of change of IT^{PlxnD1} activities from FLA and FLP centered to PIM onset (781 trials in 23 sessions from 6 mice each, two-sided Wilcoxon rank sum test *(U=528860, z=-9.14, p=6e-20*).
k. Single trial heat maps of IT^{PlxnD1} and PT^{Fezf2} activities within parietal, frontal, FLP and FLA nodes centered to PIM (IT^{PlxnD1} - 23 sessions from 6 mice, PT^{Fezf2} - 24 sessions from 5 mice).
l. Mean IT^{PlxnD1} and PT^{Fezf2} temporal dynamics within parietal (light brown), frontal (dark brown), FLP (Orange) and FLA (Magenta) centered to PIM. Grey dashed lines indicate median onset times of lick and hand lift relative to PIM (IT^{PlxnD1} - 23 sessions from 6 mice, PT^{Fezf2} - 24 sessions from 5 mice, shading around trace ±2 s.e.m). Left Inset: Overlaid activity maps of IT^{PlxnD1} (Blue) and PT^{Fezf2} (green) after thresholding indicating distinct nodes preferentially active during the feeding sequence.
m. Distribution of IT^{PlxnD1} and PT^{Fezf2} activities centered at PIM onset from parietal, frontal, FLP and FLA node and projected to the subspace spanned by the first two linear discriminant analysis dimensions (IT^{PlxnD1} - 23 sessions from 6 mice, PT^{Fezf2} - 24 sessions from 5 mice).

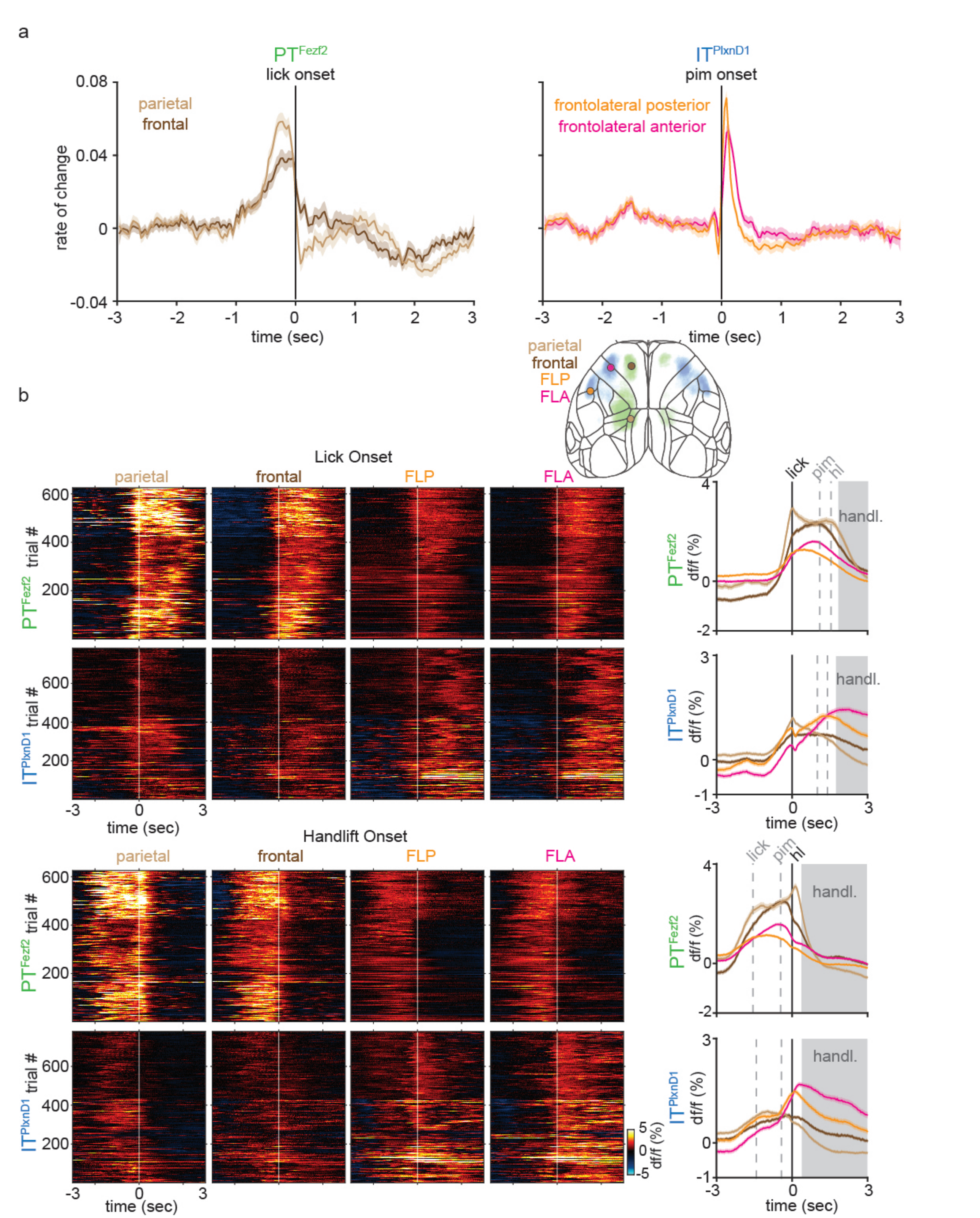

Extended data 6

Extended Data 6. Temporal dynamics of IT^{PlxnD1} and PT^{Fezf2} within pareitofrontal and frontolateral networks centered to lick and hand lift onset.

a. Mean rate of change of PT^{Fezf2} (24 sessions from 5 mice) activity centered to lick onset from parietal (light brown) and frontal (dark brown) node (left) and IT^{PlxnD1} (23 sessions from 6 mice) activity centered to pellet in mouth onset from FLA (magenta) and FLP (orange).
b. Single trial heat maps and mean activity of PT^{Fezf2} and IT^{PlxnD1} from parietal, frontal, FLA and FLP centered to lick (top) and handlift onset (bottom).

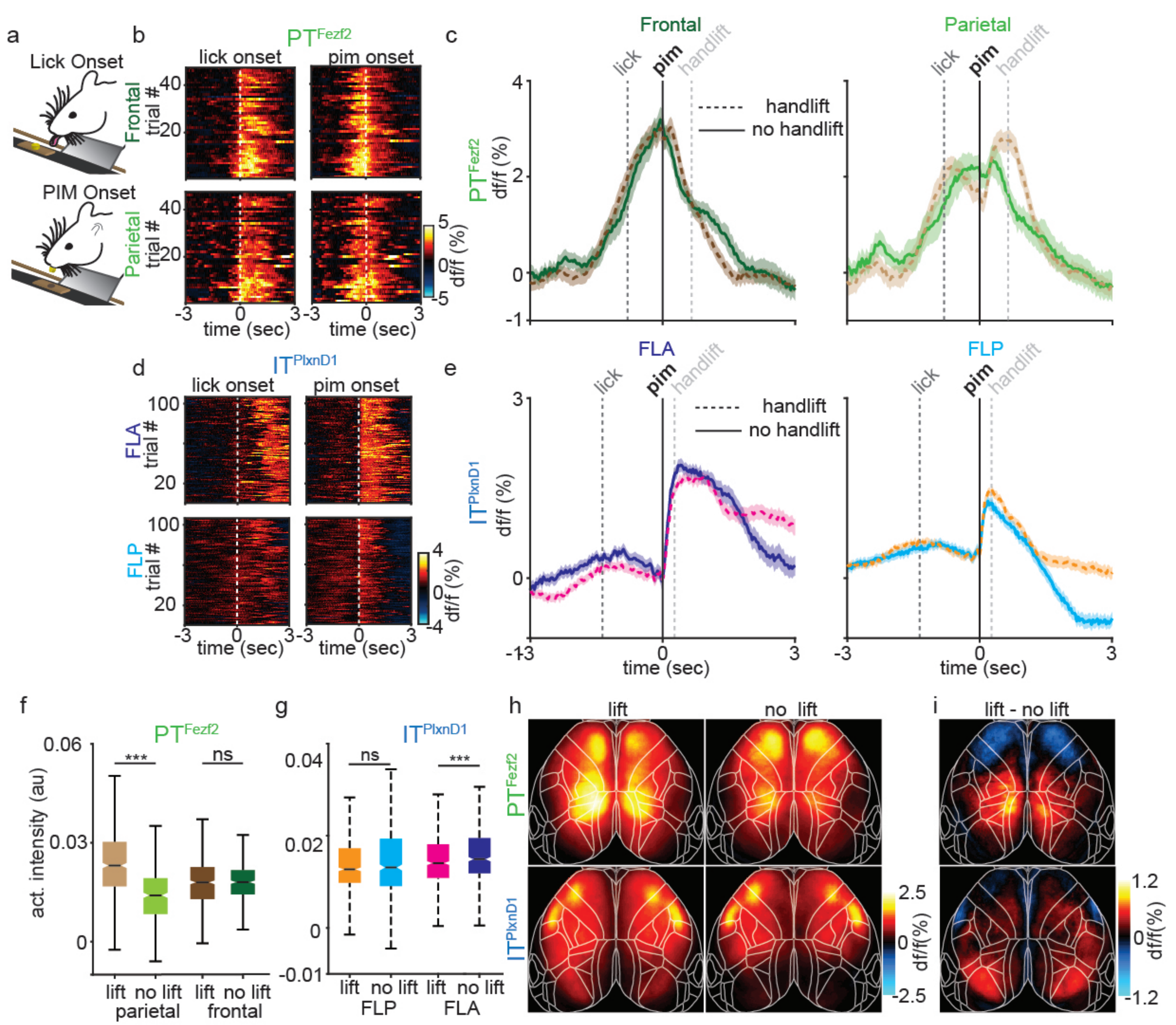
a
Lick Onset
PIM Onset
b
PT Fezf2
lick onset
pim onset
Frontal
Parietal
trial #
time (sec)
df/f (%)
c
Frontal
Parietal
lick
pim
handlift
handlift
no handlift
PT Fezf2
df/f (%)
time (sec)
d
IT PlxnD1
FLA
FLP
e
FLA
FLP
IT PlxnD1
f
PT Fezf2
act. intensity (au)
***
ns
lift
no lift
parietal
frontal
g
IT PlxnD1
ns
***
FLP
FLA
h
lift
no lift
i
lift - no lift
df/f(%)

figure 4

Figure 4. Feeding without hand lift selectively occludes PT^{Fezf2} activity in parietal node.

a. Schematic of feeding without hand following preventing hand lift with a blocking plate.
b. Single trial heat maps of PT^{Fezf2} activity within frontal and parietal nodes centered to onset of licking and PIM during feeding without hand lift (2 sessions from one example mouse).
c. Mean ^{PTFezf2} activity within frontal (left) and parietal (right) nodes centered to onset of PIM during feeding with (frontal: dark brown, parietal: light brown, 5 sessions from one example mouse, shading around trace ±2 s.e.m) and without handlift (frontal: dark green, parietal: light green, 2 sessions from the same example mouse, shading around trace ±2 s.e.m).
d. Single trial heat maps of IT^{PlxnD1} activity within FLA and FLP centered to onset of licking and PIM during feeding without hand (3 sessions from one example mouse).
e. Mean IT^{PlxnD1} activity within frontolateral anterior (left) and frontolateral posterior (right) nodes centered to onset of PIM during feeding with (FLA: magenta, FLP: orange, 5 sessions from one example mouse, shading around trace ±2 s.e.m) and without hand lift (FLA: dark blue, FLP: cyan, 3 sessions from the same example mouse, shading around trace ±2 s.e.m).
f. Distribution of PT^{Fezf2} activity intensity during 1 sec post PIM onset from parietal and frontal nodes across behaviors with and without hand (no lift: 440 trials in 13 sessions from 5 mice, lift: 647 trials in 24 sessions from the same 5 mice, two-sided Wilcoxon rank sum test, parietal node *(U=466068, z=14.6, p=3.4e-48)*, frontal node *(U=347465, z=-0.88, p=0.37)*).
g. Distribution of IT^{PlxnD1} activity intensity during 1 sec post PIM onset from FLA and FLP across behaviors with and without hand (no lift: 544 trials in 15 sessions from 6 mice, lift: 781 trials in 23 sessions from the same 6 mice, two-sided Wilcoxon rank sum test, FLP *(U=512068, z=-0.84, p=0.4)*, FLA *(U=495163, z=-3.3, p=9e-4)*).
h. Mean PT^{Fezf2} (top) and IT^{PlxnD1} (bottom) spatial activity maps during 1 second post PIM onset for behaviors with (left) and without (right) hand.
i. Difference in PT^{Fezf2} (top) and IT^{PlxnD1} (bottom) mean spatial activity maps between eating with and without hand.

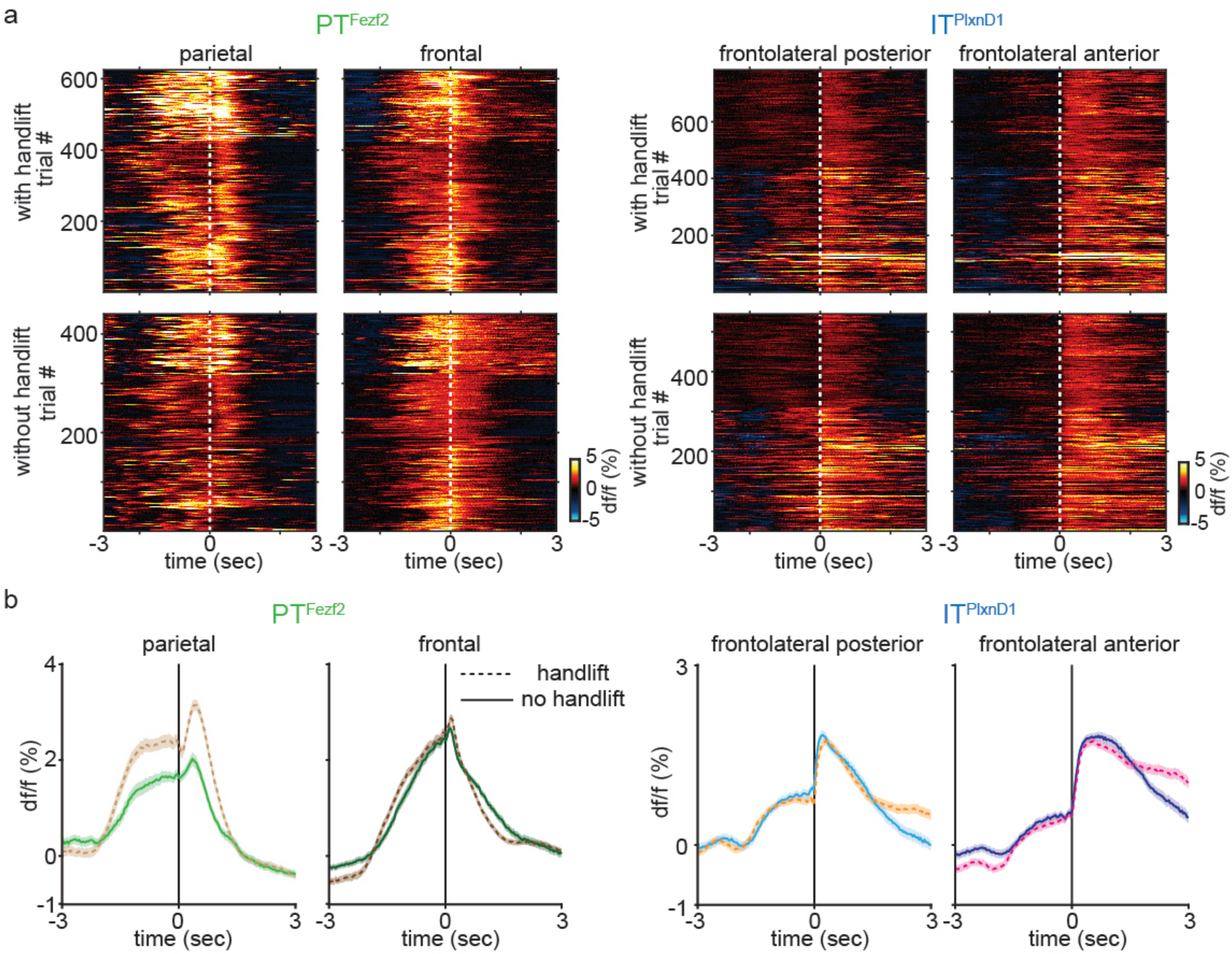

Extended data 7

Extended Data 7. Temporal dynamics of IT^{PlxnD1} in frontolateral and PT^{Fezf2} within parietofrontal nodes during feeding with and without hand lift across mice.

a. Single trial heat maps of PT^{Fezf2} activity centered to pellet in mouth onset from parietal and frontal node and IT^{PlxnD1} activity in FLP and FLA from eating with (top) and without hand lift (bottom) from all mice and sessions (With handlift : IT^{PlxnD1} - 23 sessions from 6 mice, PT^{Fezf2} - 24 sessions from 5 mice. Without hand lift: IT^{PlxnD1} - 15 sessions from 6 mice, PT^{Fezf2} - 13 sessions from 5 mice).
b. Left: Mean PT^{Fezf2} activity aligned to pellet in mouth onset from parietal node with (light brown) and without (light green) hand lift, frontal node with (dark brown) and without (dark green) hand lift. Right: IT^{PlxnD1} activity aligned to PIM onset from FLP with (orange) and without (cyan) hand lift and FLA with (magenta) and without (dark blue) hand lift.

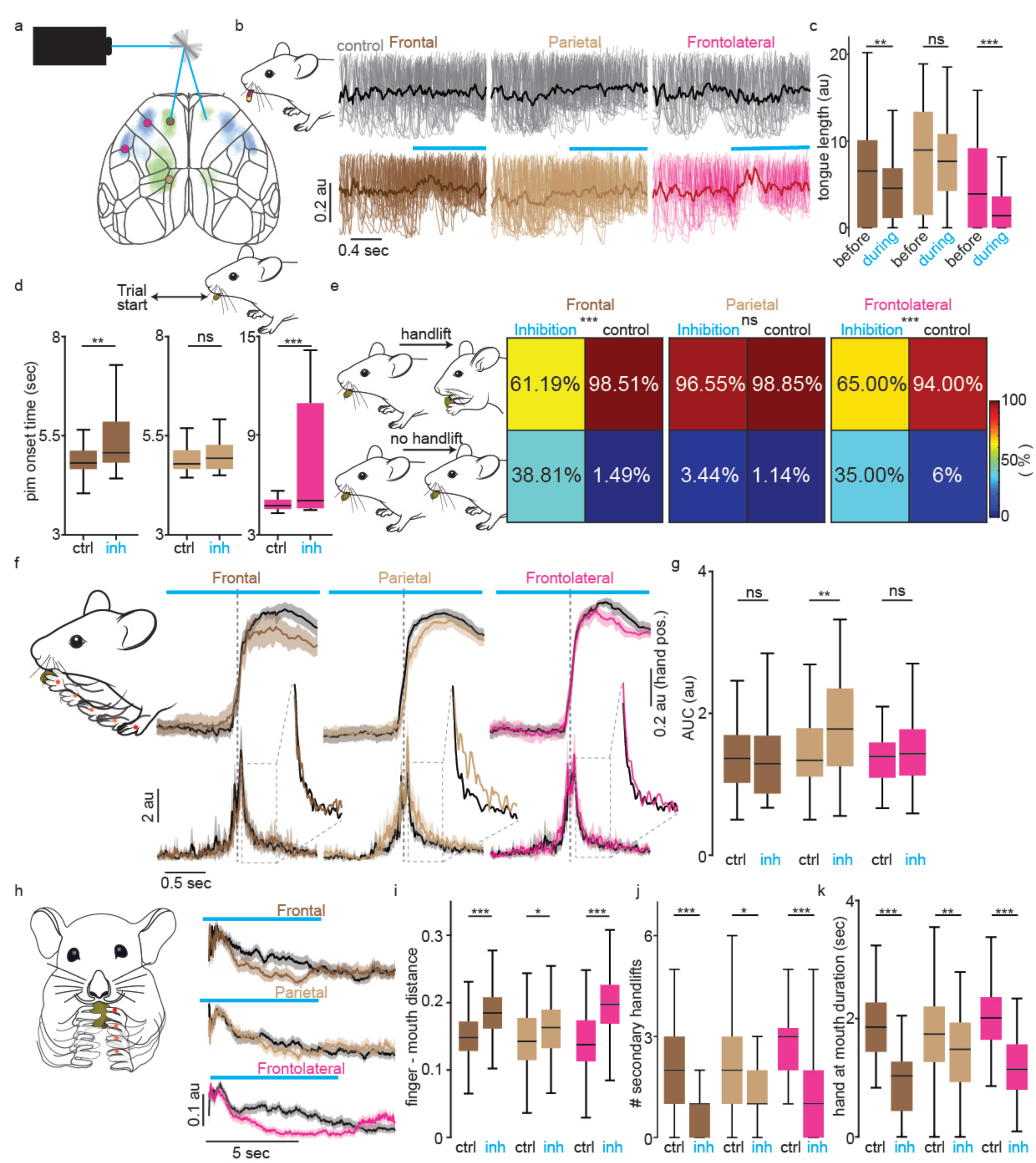
a
b
control
Frontal
Parietal
Frontolateral
0.2 au
0.4 sec
c
tongue length (au)
before
during
d
Trial start
pim onset time (sec)
ctrl
inh
e
handlift
no handlift
Frontal
Parietal
Frontolateral
Inhibition
control
61.19%
98.51%
96.55%
98.85%
65.00%
94.00%
38.81%
1.49%
3.44%
1.14%
35.00%
6%
(%)
f
2 au
0.5 sec
0.2 au (hand pos.)
g
AUC (au)
h
0.1 au
5 sec
i
finger - mouth distance
j
secondary handlifts
k
hand at mouth duration (sec)

figure 5

Figure 5. Inhibition of Parietofrontal and frontolateral subnetworks differentially disrupts sensorimotor components of feeding behavior

a. Schematic of optogenetic laser scanning setup.
b. Single trial (translucent) and averaged (opaque) tongue trajectories centered to bilateral inhibition (bottom row) of frontal (dark brown), parietal (light brown) and frontolateral (magenta, pooled across FLA and FLP) nodes. Grey trajectories (top row) are from control trials preceding inhibition trials (n = 3 mice).
c. Distribution of total tongue length 0.5 seconds before and after inhibition onset of frontal (dark brown), parietal (light brown) and frontolateral (magenta) nodes (paired two-sided Wilcoxon signed rank test, pooled from 3 mice across 7 sessions, 76 trials from frontal *(U=1522, z=3.22, p=0.0013)*, 88 trials from parietal *(U=1919, z=1, p=0.31)*, 89 trials from frontolateral *(U=1895 ,z=4.72 , p=2.3e-6)*).
d. Distribution of durations to pick pellet after trial start during control trials versus inhibition of frontal (dark brown), parietal (light brown), and frontolateral (magenta) nodes (two-sided Wilcoxon rank sum test, pooled from 3 mice across 7 sessions, 76 trials from frontal *(U=5393.5, z=3.32, p=9.13e-4)*,88 trials from parietal *(U=5919, z=0.67, p=0.5)*, 89 trials from, frontolateral *(U=6867, z=3.52, p=4.3e-4)*).
e. Probability of hand lift events during bilateral inhibition of frontal, parietal frontolateral nodes compared to control (chi-Squared test, pooled from 3 mice across 7 sessions, 67 trials from frontal *(χ^2=28.99, p=7.2e-8)*, 87 trials from parietal *(χ^2=1.02, p=0.31)*, 100 trials from frontolateral *(χ^2=25.80, p=3.78e-7)*).
f. Mean vertical hand trajectory from side view (top, shading around trace 2 s.e.m) and absolute velocity (bottom, shading around trace 2 s.e.m) while lifting hand to mouth during control (black) and inhibition of frontal (dark brown), parietal (light brown) and frontolateral (magenta) nodes. Insets indicate zoomed in mean signals. Notice increase in velocity fluctuation during parietal inhibition.
g. Distribution of the integral of absolute velocity signal for 1 second post hand lift during control and inhibition of frontal (dark brown), parietal (light brown, p<0.005 Wilcoxon rank sum test) and frontolateral (magenta) nodes (two-sided Wilcoxon rank sum test, pooled from 3 mice across 7 sessions, 41 trials from frontal *(U=1769 , z=0.62, p=0.53)*, 83 trials from parietal *(U=5872, z=-3.42, p=6.3e-4)*, 59 trials from frontolateral *(U=3356, z=-0.82, p=0.41)*)
h. Mean normalized vertical trajectory of left finger from the front view after licking pellet into mouth during control trials (black, shading around trace 2 s.e.m) and inhibition of frontal (dark brown), parietal (light brown) and frontolateral (magenta) nodes.
i. Distribution of mean normalized finger to mouth distance during control versus inhibition of frontal (dark brown), parietal (light brown) and frontolateral (magenta) nodes (two-sided Wilcoxon rank sum test, pooled from 3 mice across 7 sessions, 58 trials from frontal *(U=2545, z=-4.68, p=2.87e-6)*, 89 trials from parietal *(U=7222, z=-2.16, p=0.03)*, 101 trials from frontolateral *(U=6925, z=-7.98, p=1.43e-15)*).
j. Distribution of number of secondary hand lifts during control versus inhibition of frontal (dark brown), parietal (light brown) and frontolateral (magenta) nodes (two-sided Wilcoxon rank sum test, pooled from 3 mice across 7 sessions, 58 trials from frontal

(U=4346 , z=5.43, p=5.59e-8),89 trials from parietal *(U=8775, z=2.44, p=0.015)*, 101 trials from frontolateral *(U=12938, z=6.6, p=4e-11)*).

k. Distribution of duration of hand held close to mouth during control versus inhibition of frontal (dark brown), parietal (light brown) and frontolateral (magenta) nodes (two-sided Wilcoxon rank sum test, pooled from 3 mice across 7 sessions, 58 trials from frontal *(U=4702 , z=7.22, p=4e-13)*, 89 trials from parietal *(U=9065.5, z=3.2, p=0.0014)*, 101 trials from frontolateral *(U=13976, z=8.96, p=3e-19)*).

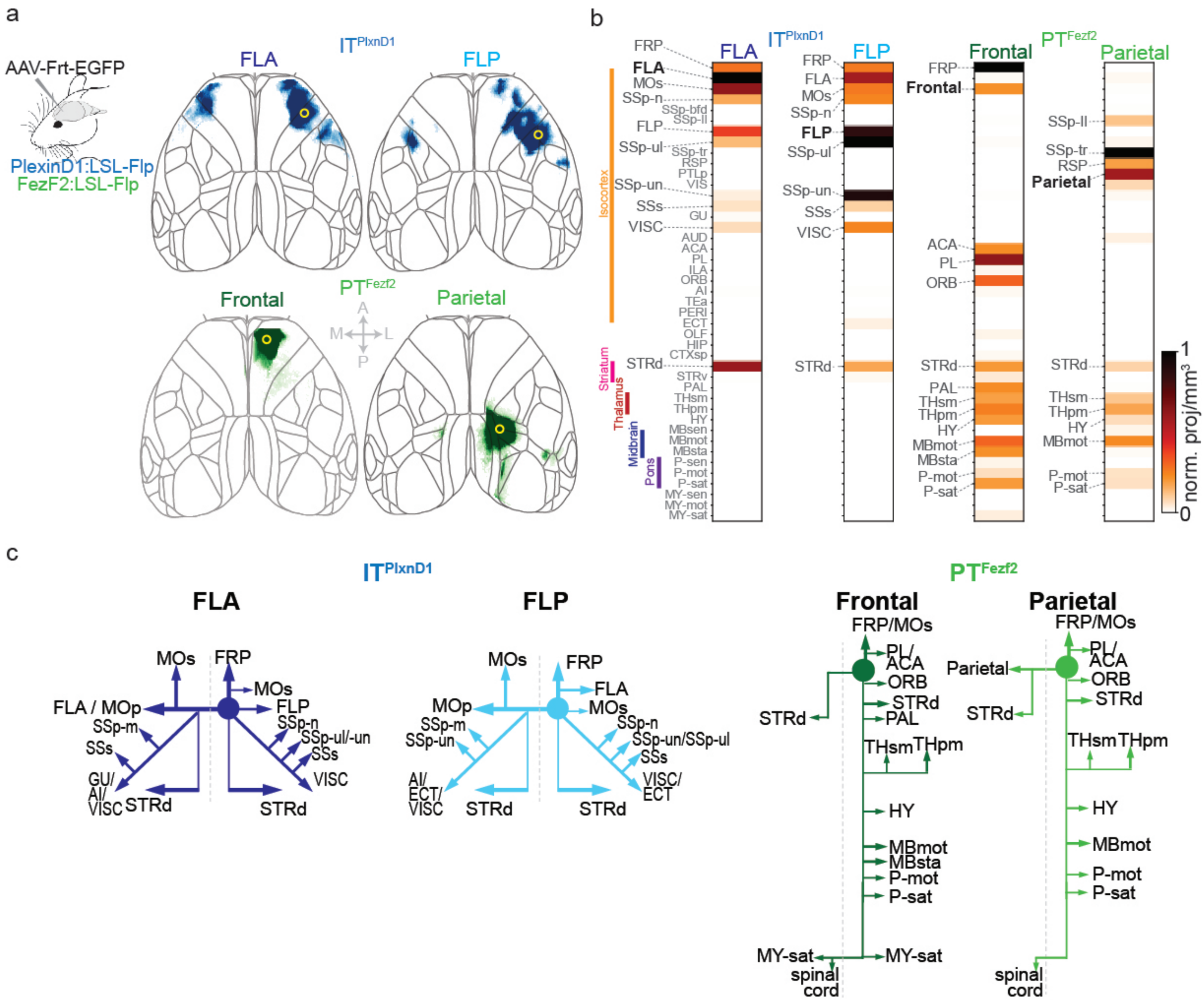
a
AAV-Frt-EGFP
PlexinD1:LSL-Flp
FezF2:LSL-Flp
IT PlxnD1
FLA
FLP
PT Fezf2
Frontal
Parietal
A
M
L
P
b
FLA
FLP
Frontal
Parietal
Isocortex
Striatum
Thalamus
Midbrain
Pons
FRP
FLA
MOs
SSp-n
SSp-bfd
SSp-ll
FLP
SSp-ul
SSp-tr
RSP
PTLp
VIS
SSp-un
SSs
GU
VISC
AUD
ACA
PL
ILA
ORB
AI
TEa
PERI
ECT
OLF
HIP
CTXsp
STRd
STRv
PAL
THsm
THpm
HY
MBsen
MBmot
MBsta
P-sen
P-mot
P-sat
MY-sen
MY-mot
MY-sat
norm. proj/mm³
1
0
c
IT PlxnD1
PT Fezf2
FLA
FLP
Frontal
Parietal
MOs
FRP
FLA / MOp
SSp-m
SSs
GU/
AI/
VISC
STRd
FLP
SSp-n
SSp-ul/-un
VISC
MOp
SSp-un
AI/
ECT/
VISC
FLA
SSp-un/SSp-ul
VISC/
ECT
FRP/MOs
PL/
ACA
ORB
PAL
THsm
THpm
HY
MBmot
MBsta
P-mot
P-sat
MY-sat
spinal
cord

figure 6

Figure 6. Brain wide projections of IT^{PlxnD1} and PT^{Fezf2} from frontolateral and parietofrontal networks.

a. Anterograde projections of IT^{PlxnD1} from FLA and FLP and PT^{Fezf2} from frontal and parietal nodes within isocortex projected to the dorsal cortical surface from an example mouse.
b. Brain-wide volume and peak normalized projection intensity maps of IT^{PlxnD1} from FLA and FLP and PT^{Fezf2} from frontal and parietal nodes from an example mouse. Black font indicates injection site; larger gray font indicate regions with significant projections; smaller gray font indicate regions analyzed.
c. Schematic of the projection of IT^{PlxnD1} from FLA and FLP and PT^{Fezf2} from Frontal and Parietal nodes. Circle indicates the site of injection.

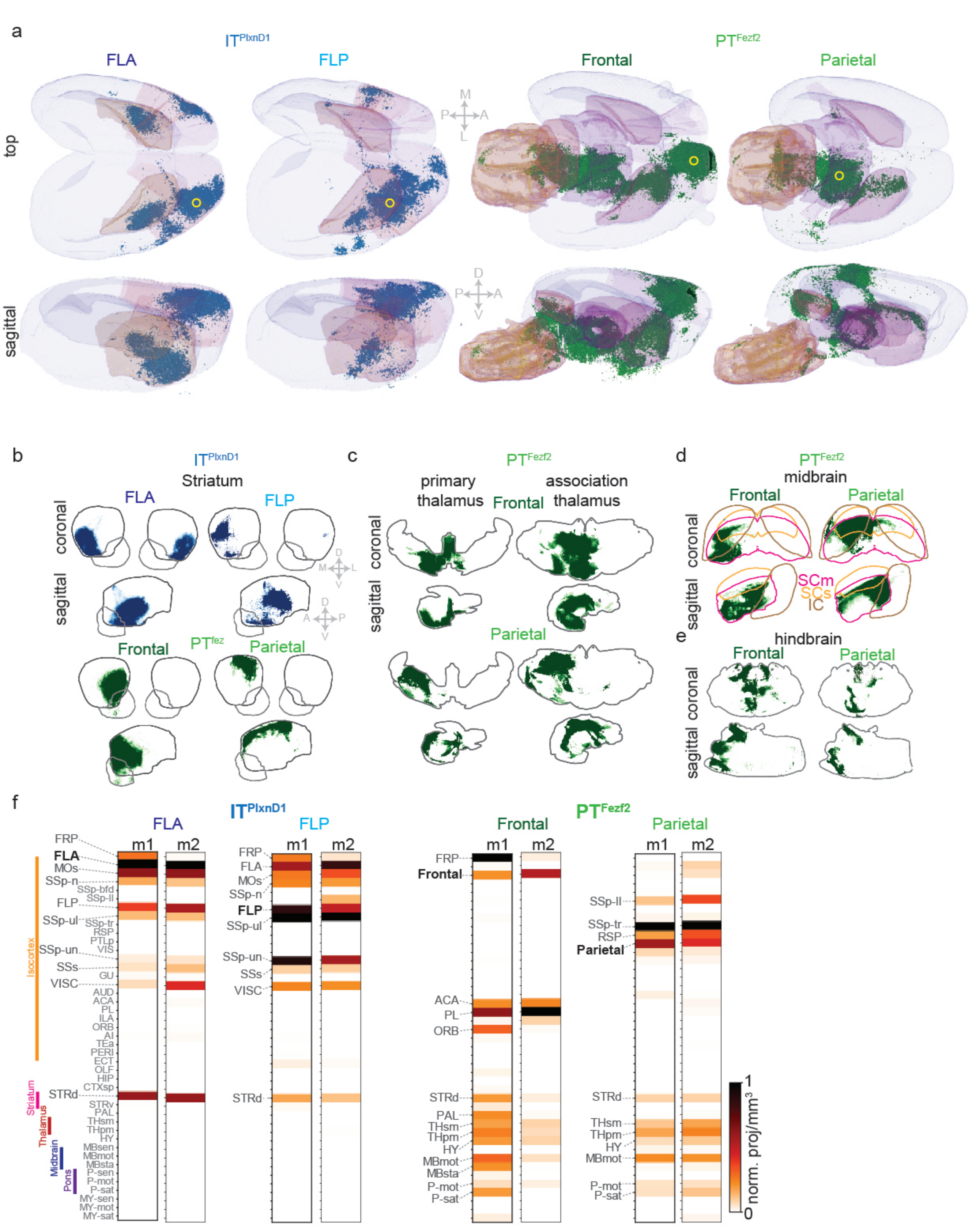

Extended data 8

Extended Data 8. Axonal projection maps in subcortical structures.

a. Three dimensional rendering of axonal projections of IT^{PlxnD1} from FLA and FLP and PT^{Fezf2} from Frontal and Parietal node. Yellow circle indicates injection site.
b. Spatial distribution of axonal projections of IT^{PlxnD1} from FLA and FLP (top) and PT^{Fezf2} parietal and frontal nodes (bottom) within the striatum projected onto the coronal and sagittal plane.
c. Spatial distribution of axonal projections of PT^{Fezf2} from parietal and frontal nodes within the primary and association thalamus projected onto the coronal and sagittal plane.
d. Spatial distribution of axonal projections of PT^{Fezf2} from parietal and frontal nodes within the motor Superior colliculus (SCm, magenta), sensory superior colliculus (SCs, yellow) and inferior colliculus (IC, brown) projected onto the coronal and sagittal plane.
e. Spatial distribution of axonal projections of PT^{Fezf2} from parietal and frontal nodes (bottom) within the hindbrain projected onto the coronal and sagittal plane.
f. Brain-wide volume and peak normalized projection intensity maps of IT^{PlxnD1} from FLA and FLP and PT^{Fezf2} from frontal and parietal nodes from two mice. Black font indicates injection site; larger gray font indicate regions with significant projections; smaller gray font indicate regions analyzed.

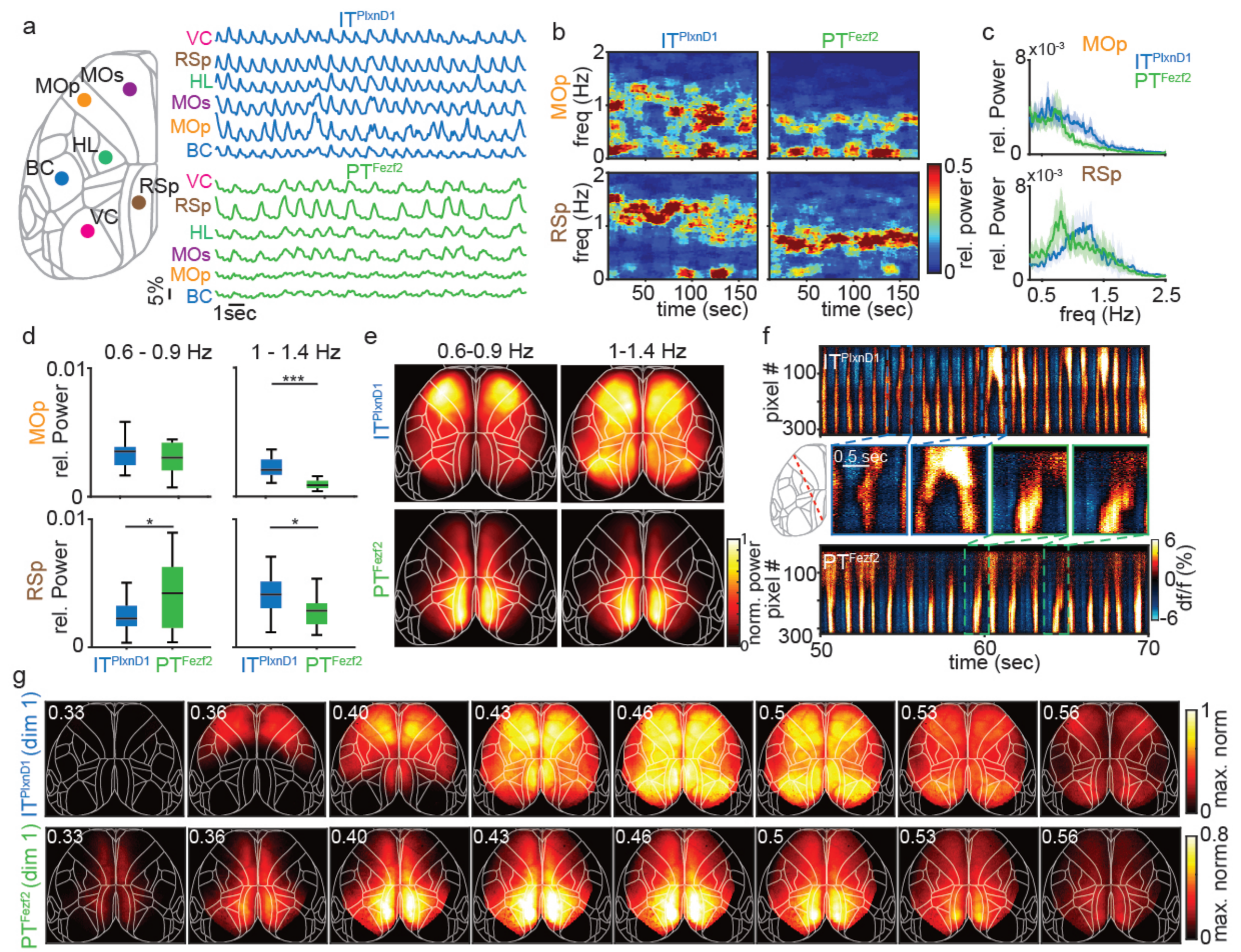
a
MOp
MOs
HL
BC
RSp
VC
IT PlxnD1
PT Fezf2
5%
1sec
b
IT PlxnD1
PT Fezf2
MOp freq (Hz)
RSp freq (Hz)
time (sec)
rel. power
c
MOp
RSp
rel. Power
freq (Hz)
d
0.6 - 0.9 Hz
1 - 1.4 Hz
MOp rel. Power
RSp rel. Power
***
*
e
0.6-0.9 Hz
1-1.4 Hz
norm. power
f
pixel #
0.5 sec
df/f (%)
time (sec)
g
0.33
0.36
0.40
0.43
0.46
0.5
0.53
0.56
max. norm

figure 7

Figure 7. IT^{PlxnD1} and PT^{Fezf2} show distinct spatiotemporal dynamics and spectral properties under ketamine anesthesia.

a. Example single trial traces of IT^{PlxnD1} and PT^{Fezf2} activities from 6 different cortical areas during ketamine/xylazine anesthesia. Colors represent cortical areas as indicated (VC- primary visual Cortex, RSp- medial retrosplenial cortex, HL – primary hindlimb sensory cortex, MOs – secondary motor Cortex, MOp – primary motor cortex, BC – barrel cortex).
b. Example spectrogram of IT^{PlxnD1} and PT^{Fezf2} activity from MOp and RSp of one mouse.
c. Mean relative power spectral density of IT^{PlxnD1} (blue) and PT^{Fezf2} (green) activity from MOp and RSp (18 sessions across 6 mice each, shading around trace ±2 s.e.m).
d. Distribution of average relative power within MOp and RSp of IT^{PlxnD1} and PT^{Fezf2} between 0.6–0.9 Hz and 1–1.4 Hz (18 sessions across 6 mice each, two-sided Wilcoxon rank sum test, 0.6-0.9 Hz MOp *(U=353, z=0.62, p=0.54)*, RSp *(U=266, z=-2.1, p=0.03)*, 1-1.4 Hz MOp *(U=482, z=4.7, p=2.6e-6)*, RSp *(U=400, z=2.1, p=0.03)*)
e. Spatial distribution of average relative power between 0.6–0.9 Hz and 1–1.4 Hz from IT^{PlxnD1} (top) and PT^{Fezf2} (bottom, 18 sessions across 6 mice each).
f. Example space-time plots of the neural activity across a slice of the dorsal cortex (red dashed lines) from IT^{PlxnD1} (top) and PT^{Fezf2} (bottom). Middle, zoomed-in activity from indicated top and bottom panels.
g. Example activation sequence of the most dominant pattern (1st dimension) identified by seqNMF from IT^{PlxnD1} (top) and PT^{Fezf2} (bottom).

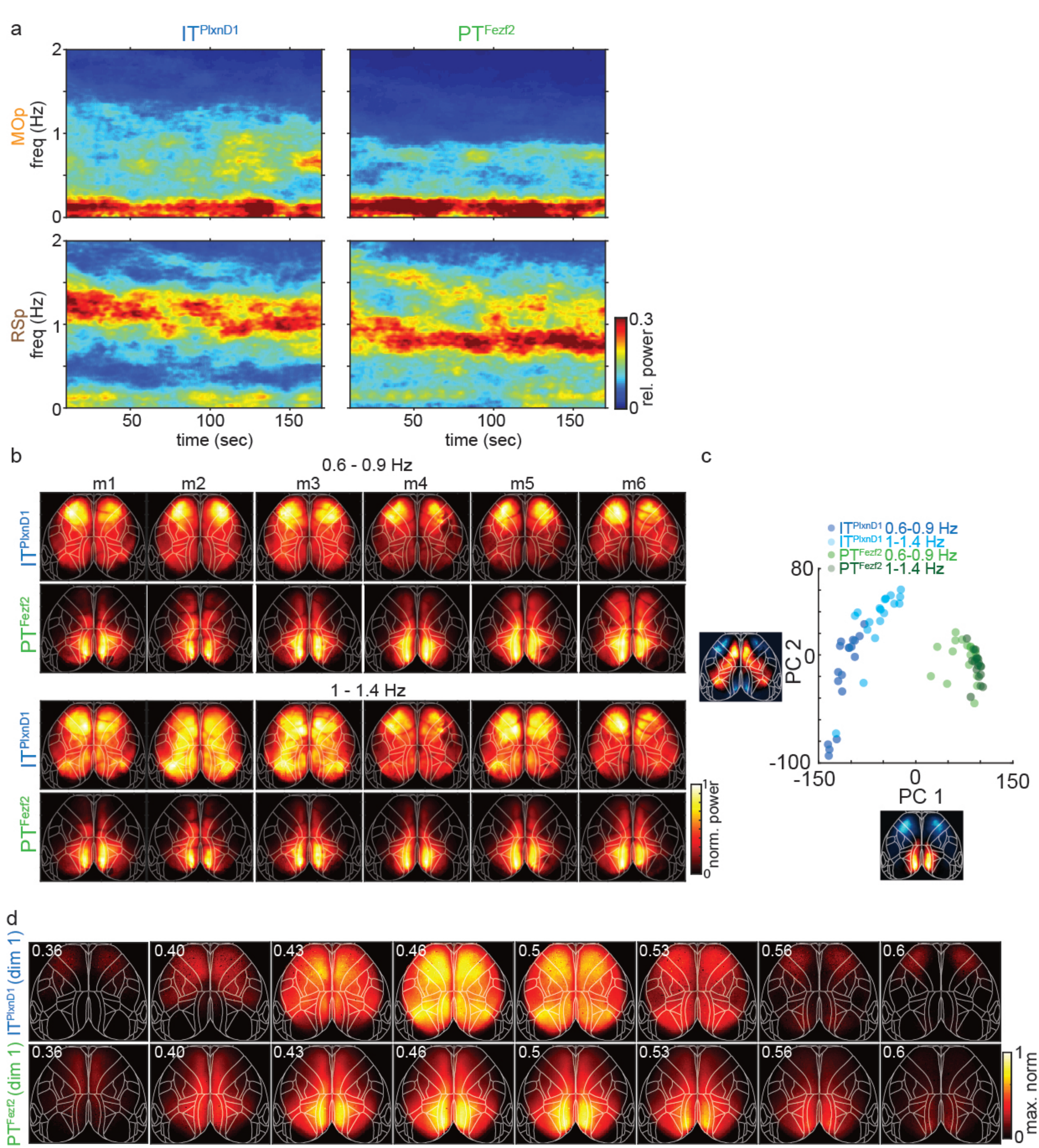

Extended data 9

Extended Data 9. Spatiotemporal dynamics of IT^{PlxnD1} and PT^{Fezf2} under ketamine anesthesia across mice.

a. Mean spectrogram of IT^{PlxnD1} and PT^{Fezf2} activity from MOp and RSp (18 sessions across 6 mice each).
b. Spatial distribution of mean relative power between 0.6–0.9 Hz (top) and 1–1.4 Hz (bottom) from IT^{PlxnD1} and PT^{Fezf2} averaged across sessions (n=3) from each mouse.
c. Distribution of IT^{PlxnD1} (blue) and PT^{Fezf2} (green) spatial power maps for each frequency band projected to the subspace spanned by the top two principal components.
d. Activation sequence of the most dominant pattern (1st dimension) identified by seqNMF from IT^{PlxnD1} (top) and PT^{Fezf2} (bottom) activity combined across mice and sessions.

Video Captions

Supplementary Video 1.

Segment of single trial calcium activity across dorsal cortex during awake resting state from one example IT^{PlxnD1} mouse (with overlaid dorsal Allen map (CCF v3)) with temporally matched behavior video frames. Each frame is indicated as quiescent or active based on behavior variance crossing a predefined threshold.

Supplementary Video 2.

Segment of single trial calcium activity across dorsal cortex during awake resting state from one example PT^{Fezf2} mouse (with overlaid dorsal Allen map (CCF v3)) with temporally matched behavior video frames. Each frame is indicated as quiescent or active based on behavior variance crossing a predefined threshold.

Supplementary Video 3.

Example video of a single trial head fixed feeding behavior with body parts tracked using deeplabcut displaying both front and side view with simultaneous traces of the tracked body parts and behavior features.

Supplementary Video 4.

Single trial calcium dynamics across dorsal cortex during head fixed feeding paradigm from one example IT^{PlxnD1} mouse with temporally matched behavior video frames from front and side view.

Supplementary Video 5.

Single trial calcium dynamics across dorsal cortex during head fixed feeding paradigm from one example PT^{Fezf2} mouse with temporally matched behavior video frames from front and side view.

Supplementary Video 6.

Video demonstrating the disruption of licking (tongue movement) on bilateral inhibition of frontolateral anterior node (FLA) in a VGAT-ChR2 mouse (Right). Video on left shows

behavior from the same mouse on the previous trial during the same period with no inhibition (control trial).

Supplementary Video 7.

Video demonstrating the obstruction of handlift onset on bilateral inhibition of frontolateral anterior node (FLA) in a VGAT-ChR2 mouse (Right). Video on left shows behavior from the same mouse on the previous trial during the same period with no inhibition (control trial).

Supplementary Video 8.

Video demonstrating the impediment in smooth movement of hand lift trajectory on bilateral inhibition of parietal node in a VGAT-ChR2 mouse (Right). Video on left shows behavior from the same mouse on the previous trial during the same period with no inhibition (control trial).

Supplementary Video 9.

Video demonstrating the impairment in proper handling and manipulation of food pellet on bilateral inhibition of frontolateral anterior node in a VGAT-ChR2 mouse (Right). Video on left shows behavior from the same mouse on the previous trial during the same period with no inhibition (control trial).

Supplementary Video 10.

Video of full brain STP imaged serial coronal sections with registered Allen map (CCF v3) overlaid from an IT^{PlxnD1} mouse injected with anterograde tracer in right frontolateral anterior node with its whole brain axonal projections.

Supplementary Video 11.

Video of full brain STP imaged serial coronal sections with registered Allen map (CCF v3) overlaid from an IT^{PlxnD1} mouse injected with anterograde tracer in right frontolateral posterior node with its whole brain axonal projections.

Supplementary Video 12.

Video of full brain STP imaged serial coronal sections with registered Allen map (CCF v3) overlaid from a PT^{Fezf2} mouse injected with anterograde tracer in right frontal node with its whole brain axonal projections.

Supplementary Video 13.

Video of full brain STP imaged serial coronal sections with registered Allen map (CCF v3) overlaid from a PT^{Fezf2} mouse injected with anterograde tracer in right parietal node with its whole brain axonal projections.

Supplementary Video 14.

Segment of single trial calcium activity across dorsal cortex during Ketamine/Xylazine anesthetized state from one example IT^{PlxnD1} mouse with overlaid dorsal Allen map (CCF v3).

Supplementary Video 15.

Segment of single trial calcium activity across dorsal cortex during Ketamine/Xylazine anesthetized state from one example PT^{Fezf2} mouse with overlaid dorsal Allen map (CCF v3).